

Properties of the twisted Polyakov loop coupling and the infrared fixed point in the SU(3) gauge theory

Etsuko Itou¹

¹*High Energy Accelerator Research Organization (KEK), Tsukuba 305-0801, Japan*

**E-mail: eitou@post.kek.jp*

.....
We report the nonperturbative behavior of the twisted Polyakov loop (TPL) coupling constant for the SU(3) gauge theory, which is one of the nonperturbative renormalized coupling constants defined in finite volume. We reveal the vacuum structures and the phase structure for the lattice gauge theory with the twisted boundary condition, and derive the nonperturbative beta function in this renormalization scheme and carry out the numerical simulations in the cases of the quenched QCD and $N_f = 12$ SU(3) theories.

At first, we study the quenched QCD theory by using the plaquette gauge action. The TPL coupling constant shows a fake fixed point in the confinement phase even in the quenched QCD. We discuss this property and show the nonperturbative running coupling constant in the deconfinement phase, where the magnitude of the Polyakov loop shows the nonzero values.

We also investigate the system coupled with fundamental fermions. We use the naive staggered fermion in our simulation, and then the minimum number of flavor is 12 in this lattice setup because of the twisted boundary condition. The $N_f = 12$ SU(3) gauge theory is expected that the running coupling constant shows a conformal behavior from the perturbative analysis. We show the vacuum structure and phase structure of this lattice setup with analytical and numerical methods, and then show the detailed analysis of the running coupling constant of this theory. Finally, we find the infrared fixed point (IRFP) and discuss the robustness of the nontrivial IRFP of many flavor system under the change of the analysis method.

A part of preliminary results was reported in the proceedings [1, 2] and the letter paper[3]. In this paper we include a review of these results and show the final conclusion for the existence of IRFP of SU(3) $N_f = 12$ massless theory using the updated data.

.....
Subject Index B32, B38, B44

1. Introduction

Lattice gauge theory is one of the most successful regularization tools to understand QCD. It can be applied even to the strong coupling region, and we can investigate the nonperturbative properties of QCD. Based on the success of the lattice QCD, there are several application for the lattice gauge theory with the different gauge group, the different number of flavor and the fermion representation. Among recent lattice studies, the search for the conformal or nearly conformal field theory in the infrared (IR) regime have been performed, motivated by both theoretical and phenomenological interests [4] – [49].

A simple way to find the conformal fixed point is to study the beta function of the theory. While the renormalized coupling constant itself is scheme dependent quantity, the existence

of the fixed point does not depend on the renormalization scheme. This is understood as follows. Let us consider a relationship between two renormalized coupling constant defined in different renormalization schemes, $g_1 = F(g_2)$. The beta functions of these two schemes are related

$$\beta(g_1) = \frac{\partial F}{\partial g_2} \beta(g_2). \quad (1.1)$$

A zero point of the beta function is thus scheme independent except for singular point of the transformations.

In the recent studies to search for the infrared fixed point (IRFP), in particular, there are many independent studies in the case of SU(3) gauge theory coupled with $N_f = 12$ fundamental fermions. The existence of the IRFP in $N_f = 12$ theory was predicted by the perturbative 2-loop beta function [50] and the further higher order analysis in the $\overline{\text{MS}}$ scheme [51]. The phase structure at IRFP was also studied in the paper [52]. Based on these analytical studies, there are several works to investigate the nonperturbative running coupling constant and the phase structures, although the results have been controversial hitherto. In Ref [8], the running coupling constant was computed in the Schrödinger functional (SF) scheme [53–55], and within error exhibited scale independent behavior in the IR at coupling $g_{SF}^{2*} \sim 5$. And the MCRG method [22, 23], the phase structure in the finite temperature system [17, 18] and the scaling behavior with mass deformed theory [10, 27] show the evidence of the IRFP. In the studies of SU(3) gauge theory with $N_f = 7$ and 10 [4, 41], they found that theory is in the conformal window which also suggest that $N_f = 12$ theory is conformal. On the other hand, the studies of the mass scaling behavior [15] and the spectrum of the Dirac operator and the chiral symmetry [12, 21] show evidence that this theory is not conformal at low energy.

One reason of the controversy may be the systematic error. In the Ref. [8], they derived the running coupling constant by taking the constant continuum extrapolation. That means the discretization effects, which is the renormalization scheme dependent, is neglected. There is no study of the running coupling constant which takes care of the discretization error carefully at least in the case of $N_f = 12$. The other reason may be the effect the bulk phase. It also depends on the lattice action. Actually, a new bulk phase in this lattice gauge theory and the importance of the avoiding bulk phase are also reported [19–21, 24].

According to these studies, it is suggested that there are two important things to verify the existence or non-existence of IRFP. The first one is to estimate the discretization effect, since the strong coupling region might have the large lattice artifact. The critical behavior appears in the continuum theory, and then careful continuum extrapolation is necessary. The second one is to study the parameter region, in particular to avoid the lattice artifact phase. The parameter region of the artifact phase depends on the lattice action, it should be studied for each lattice setup.

This work reports a study of the phase structure and the running coupling constant for SU(3) gauge theory with $N_f = 0$ and 12. We use the plaquette gauge and the naive staggered fermion actions. Firstly, we study the phase structure of these theories within both analytical and numerical methods, and then derive numerically the running coupling constant in the deconfinement phase. The renormalization scheme we chose is the twisted Polyakov loop (TPL) scheme. The TPL coupling was proposed by de Divitiis *et al.* [56] for the SU(2) case, and we extend it to the SU(3) theory. This renormalization scheme has no $O(a)$ discretization

error, which is of great advantage when we take the continuum limit. Another advantage of this scheme is the absence of zero mode contributions thanks to the twisted boundary condition [57, 58]. This regulates the fermion determinant in the massless limit, which enables simulation with massless fermions. In this work, we take the continuum limit carefully, and show the existence of the IRFP in the $N_f = 12$ theory if we include the systematic uncertainty coming from the continuum extrapolation.

In this paper, we give a definition of SU(3) TPL renormalized coupling, and the tree level calculation of the TPL coupling in Sec. 2. We show the first example of the running coupling constant in the case of quenched QCD theory in Sec. 3. We show the scaling behavior of the scheme and the nonperturbative property of the running coupling constant. The TPL coupling constant approaches to a constant if the theory is in the confinement phase. We discuss the way how to distinguish such a fake “fixed point” and the true one in this renormalization scheme in the Sec. 3.1. In Sec. 4, we discuss the vacuum structure and Z_{N_c} symmetry in the system coupled with fermions by the semi-classical analysis in the case of $N_f = 12$ theory. We also show the numerical results of the phase structure of massive and massless $N_f = 12$ SU(3) theory in Sec. 6. In Sec. 7, we study the running coupling constant for massless $N_f = 12$ case. We firstly study the global behavior of the step scaling function using the data set given in Appendix A, and then investigate the existence of the IRFP by the local fit using the additional data set (Appendix B) in the strong coupling regime. The detailed discussion for the stability of the IRFP is given in Appendix C. We also discuss the taste breaking effects in this analysis in Appendix F.

One of the main results of this paper is that we found the IRFP at

$$g_{\text{TPL}}^{*2} = 2.69 \pm 0.14 (\text{stat.})_{-0.16}^{+0} (\text{syst.}), \quad (1.2)$$

and the critical exponent of the β function around the IRFP is

$$\gamma_g^* = 0.57_{-0.31}^{+0.35} (\text{stat.})_{-0.16}^{+0} (\text{syst.}). \quad (1.3)$$

There is an independent paper using the similar idea [59]. The present work is that we add the new data showing the strong evidence of the IRFP beyond the systematic uncertainty. Data analysis is also refined in various ways as discussed below. The details of difference from the paper [59], including the discrepancy of the value of g_{TPL}^{*2} by more than $2\text{-}\sigma$, are discussed in Appendix D and E.

2. Twisted Polyakov loop (TPL) scheme

One of nonperturbative definitions for the renormalized coupling constant can be given by a divergence-free ratio (\mathcal{A}_{NP}) of nonperturbative amplitudes. If the tree level value of the quantity is proportional to the squared bare coupling constant, $\mathcal{A}_{tree} = kg_0^2$, where k is the constant which is calculated by the tree level quantity, then we can define the nonperturbative renormalized coupling constant from the nonperturbative ratio \mathcal{A}_{NP} by identifying the renormalization factor of the amplitude as the quantum correction of the coupling constant:

$$g_{NP}^2 \equiv \frac{\mathcal{A}_{NP}}{k}. \quad (2.1)$$

Since the lattice simulation gives us the value of \mathcal{A}_{NP} , what we have to do is to find a ratio of tree level amplitudes \mathcal{A}_{tree} which is proportional to the squared bare coupling constant.

Twisted Polyakov loop (TPL) scheme is one of such nonperturbative renormalized couplings defined in finite volume. This scheme is given in Ref. [56] in the case of SU(2) gauge theory, choosing the ratio of Polyakov loop expectation values for twisted and untwisted directions as the quantity \mathcal{A}_{NP} . We extend the definition in Ref. [56] to the SU(3) case. This scheme can be defined also in the continuum finite volume, however, in this section, we start a brief review of the definition of TPL scheme on the lattice.

2.1. The definition of TPL scheme in the SU(3) gauge theory

To define the TPL scheme, we introduce twisted boundary condition for the link variables (U_μ) in x and y directions and the ordinary periodic boundary condition in z and t directions on the lattice:

$$U_\mu(x + \hat{\nu}L/a) = \Omega_\nu U_\mu(x) \Omega_\nu^\dagger, \quad (2.2)$$

for $\mu = x, y, z, t$ and $\nu = x, y$. Here, Ω_ν ($\nu = x, y$) are the twist matrices which have the following properties:

$$\Omega_\nu \Omega_\nu^\dagger = \mathbb{I}, (\Omega_\nu)^3 = \mathbb{I}, \text{Tr}[\Omega_\nu] = 0,$$

and

$$\Omega_\mu \Omega_\nu = e^{i2\pi/3} \Omega_\nu \Omega_\mu, \quad (2.3)$$

for a given μ and $\nu (\neq \mu)$. The gauge transformation $U_\mu(r) \rightarrow \Lambda(r) U_\mu(r) \Lambda^\dagger(r + \hat{\mu})$ and eq.(2.2) imply

$$\Lambda(r + \hat{\nu}L/a) = \Omega_\nu \Lambda(r) \Omega_\nu^\dagger. \quad (2.4)$$

In the system coupled with fermions, we also have to define the twisted boundary conditions for fermions. The naive twisted boundary condition for lattice fundamental fermions can be written by

$$\psi(x + \hat{\nu}L/a) = \Omega_\nu \psi(x), \quad (2.5)$$

for $\nu = x, y$. However, this results in an inconsistency when changing the order of translations, namely,

$$\begin{aligned} \psi(x + \hat{\nu}L/a + \hat{\rho}L/a) &= \Omega_\rho \Omega_\nu \psi(x), \\ &\neq \Omega_\nu \Omega_\rho \psi(x), \end{aligned} \quad (2.6)$$

for $\rho, \nu = x, y$. To avoid this difficulty, we introduce a “smell” symmetry [61], which can be realized by an integral multiple of color symmetry, $N_s = n_s \times N_c$, where N_c and N_s are the degree of color and smell symmetry respectively. We identify the fermion field as a $N_c \times N_s$ matrix ($\psi_\alpha^a(x)$), here a and α denote the indices of the color and smell and they run $a = 1, \dots, N_c$ and $\alpha = 1, \dots, N_s$. Then we impose the twisted boundary condition for fermion fields as

$$\psi_\alpha^a(x + \hat{\nu}L/a) = e^{i\pi/3} \Omega_\nu^{ab} \psi_\beta^b(\Omega_\nu)_{\beta\alpha}^\dagger \quad (2.7)$$

for $\nu = x, y$ directions. Here, the smell index can be considered as a “flavor” index, then the number of flavors should be a multiple of $N_s (= N_c = 3)$. We use staggered fermion in our

simulation. This contains four tastes for each flavor. This restrict the number of flavors to multiples of 12 in this SU(3) gauge theory with twisted boundary condition.

Finally, we define the renormalized coupling constant of the TPL scheme. Because of this twisted boundary condition, the definition of Polyakov loops in the twisted directions are modified as,

$$P_x(y, z, t) = \text{Tr} \left(\left[\prod_j U_x(x = j, y, z, t) \right] \Omega_x e^{i2\pi y/3L} \right), \quad (2.8)$$

in order to satisfy gauge invariance and translational invariance. The renormalized coupling in the TPL scheme is defined by taking a ratio of Polyakov loop correlators in the twisted (P_x) and untwisted (P_z) directions:

$$g_{\text{TPL}}^2 = \lim_{a \rightarrow 0} \frac{1}{k_{\text{latt}}} \frac{\langle \sum_{y,z} P_x(y, z, L/2a) P_x(0, 0, 0)^\dagger \rangle}{\langle \sum_{x,y} P_z(x, y, L/2a) P_z(0, 0, 0)^\dagger \rangle}. \quad (2.9)$$

At tree level, this ratio of Polyakov loops is proportional to the bare coupling. The proportionality factor on the lattice (k_{latt}) is obtained by analytically calculating the one-gluon-exchange diagram. To perform this analytic calculation, we choose the explicit form of the twist matrices [62],

$$\Omega_x = \begin{pmatrix} 0 & 1 & 0 \\ 0 & 0 & 1 \\ 1 & 0 & 0 \end{pmatrix}, \Omega_y = \begin{pmatrix} e^{-i2\pi/3} & 0 & 0 \\ 0 & e^{i2\pi/3} & 0 \\ 0 & 0 & 1 \end{pmatrix}. \quad (2.10)$$

The Feynman rule for the SU(N_c) gauge theory on the lattice with the twisted boundary condition is given in Appendix B in the paper [56]. The value of k_{latt} is given as

$$k_{\text{latt}} = \frac{1}{g^2 N_c} \frac{1}{\hat{L}^2} \sum_{\hat{k}_\mu} \frac{\exp(i\hat{k}^{ph} \cdot \hat{r})}{\sum_\mu \sin^2(\hat{k}_\mu/2)}, \quad (2.11)$$

here $\hat{L} = L/a$, $\hat{r} = (x, y, z, L/2a)$ and \hat{k}_μ denotes the momentum in each direction. In the twisted direction, it gives the sum of the physical and the unphysical twisted momentum:

$$\begin{aligned} \hat{k}_{x,y} &= \hat{k}_{x,y}^{ph} + \hat{k}_{x,y}^\perp, \\ &= \frac{2\pi n_{x,y}^{ph}}{\hat{L}} + \frac{\pi(2m_{x,y}^\perp + 1)}{3\hat{L}}, \\ \hat{k}_{z,t} &= \hat{k}_{z,t}^{ph}, \\ &= \frac{2\pi n_{z,t}^{ph}}{\hat{L}}, \end{aligned} \quad (2.12)$$

where $n_\mu^{ph} = 0, \dots, \hat{L}/2 - 1$ and $m_{x,y}^\perp = 0, 1, \dots, N_c - 1$ with $(m_x^\perp, m_y^\perp) \neq (0, 0)$. The momentum \hat{k}^\perp can be identified as the color degree of freedom ($N_c^2 - 1$) in the color basis (see: the Appendix B in the paper [56]).

L/a	k_{latt}
4	0.03213022128143844
6	0.03196454161502177
8	0.03191145402091543
10	0.03188777626443608
12	0.03187515361346823
16	0.03186277699696222
20	0.03185710526062057

Table 1 The value of k_{latt} for $L/a = 4, 6, 8, 10, 12, 16, 20$ for SU(3) gauge theory.

In the continuum limit the proportional factor (k) for SU(3) gauge theory is calculated analytically as:

$$\begin{aligned}
k &= \frac{1}{24\pi^2} \sum \frac{(-1)^n}{n^2 + (1/3)^2} \\
&= \frac{1}{24\pi^2} \left[\frac{9}{2} - \frac{3\pi}{2} \operatorname{cosech} \left(\frac{\pi}{3} \right) \right] \\
&= 0.03184 \dots
\end{aligned} \tag{2.13}$$

The values of k_{latt} in Table 1 can be fitted by a linear function of $O(a^2)$ instead of $O(a)$, as expected.

3. The TPL coupling for the quenched QCD

In this section, we study the TPL coupling constant in the quenched QCD. In the first subsection, we discuss the property of TPL coupling in the quenched theory and investigate the parameter region where the study of the TPL coupling makes sense. We show the running coupling constant for the quenched QCD in Sec. 3.2.

3.1. Phase structure and TPL coupling constant

The TPL coupling constant is defined by taking the ratio of the Polyakov loop correlators between the twisted and the untwisted directions. If the theory is in the confinement phase, for sufficiently the correlation length of the Polyakov loop is shorter than the volume and the gluon does not feel the boundary effect. We can expect that the ratio of the Polyakov loop correlators becomes 1, and we can not extract of the running behavior in such region. The quenched QCD theory shows the confinement/deconfinement phase transition in the finite volumes, and we can use the TPL running coupling only in the deconfinement phase, where the magnitude of the Polyakov loop shows nonzero values.

To see this property, we observe β dependence ($\beta \equiv 6/g_0^2$ where g_0 is the bare coupling constant) of the TPL coupling constant at fixed lattice sizes. Apart from discretization errors the scale increases as the β decreases at a fixed lattice size. In this test, we use smaller lattice sizes, $L/a = 2 - 6$, with relatively low β values. The configurations are generated by the Hybrid Monte Carlo algorithm and the action is the Wilson plaquette. We measure the Polyakov loop and its correlator for every Monte Carlo trajectory, and each data statistics has the same: 20,000 trajectories. The size of error bar shows the statistical fluctuation at the same statistics.

The measured TPL coupling constant and the absolute value of the Polyakov loop in t -direction are presented in Fig. 1¹. The top panels denote the absolute values of the Polyakov loop and the bottom ones denote the corresponding TPL coupling scaled by the coefficient k_{latt} for each lattice size. We found that the absolute value of the Polyakov loop approaches zero in the low energy region. The confinement/deconfinement phase transition occurs and the transition point of β depends on the lattice size. From the bottom panels, we can see the ratio of Polyakov loop ($k_{latt}g_{TPL}^2$) becomes unity below the transition point.

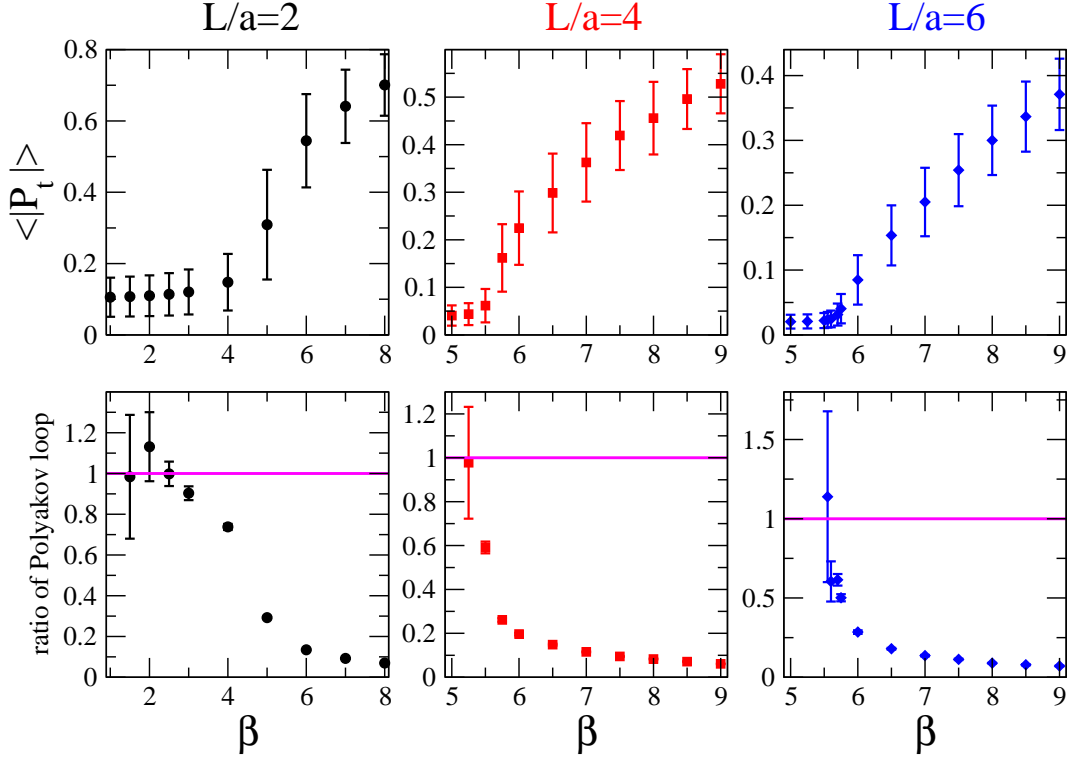


Fig. 1 The ratio of Polyakov loop and the absolute value of Polyakov loop in t direction for $L/a = 2, 4$ and 6 .

There is a question whether we can use this TPL scheme for the conformal fixed point search in IR region. One discrimination method is to check the value of renormalized coupling, although the value of the renormalized coupling at the fixed point is scheme dependent. Assume that a theory has IRFP. The fake fixed point appears at $g_{TPL}^2 \sim 1/k \sim 32$. If there is an IRFP at $g_{TPL}^{2*} \neq 1/k \sim 32$, then we can discuss the fixed point as a physical fixed point. On the other hand, if the true fixed point value of the renormalized coupling in the TPL scheme is larger than $1/k$, then we will not reach that point. The other important check is to see the phase structure of the theory at the same time. At the true conformal fixed point, the theory must be in the deconfinement phase. There is a possibility of the

¹ We drop the data of the ratio of Polyakov loop for $\beta = 1.0, L/a = 2$, $\beta = 5.0, L/a = 4$ and $\beta \leq 5.5, L/a = 6$, since these error bars become huge. Of course, they are consistent with 1.

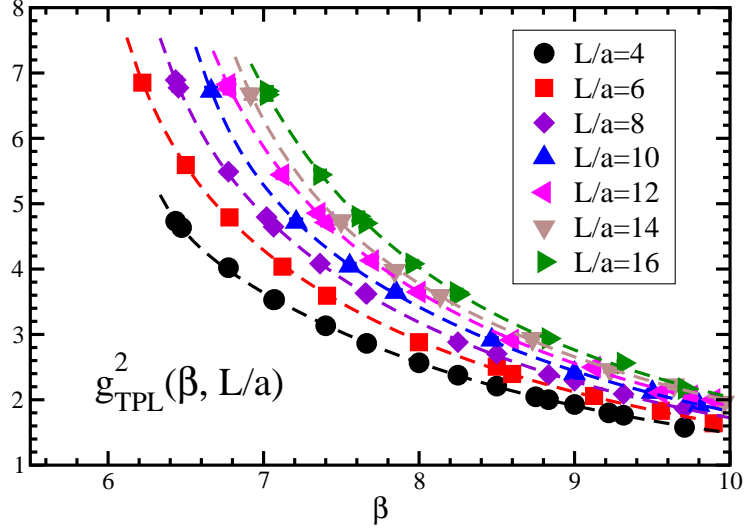


Fig. 2 TPL renormalized coupling in the each β and L/a in quenched QCD. Dashed lines express fit lines of fixed L/a as a function of β .

existence of the bulk phase in the low β region, in which the Polyakov loop shows the confinement and/or chiral symmetry broken behavior [19, 20, 24], if the lattice theory includes the dynamical fermions. We discuss this point in the case of $N_f = 12$ in Sec. 6.

3.2. Running coupling constant for quenched QCD

Now, we would like to show the running coupling constant for quenched QCD. The main result was already reported in [1] Here we would extend discussions. The gauge configurations in this subsection are generated by the pseudo-heatbath algorithm and overrelaxation algorithm mixed in the ratio 1:5. One combination of the pseudo-heatbath and 5 overrelaxation steps called a “sweep” in the following. In order to generate the configurations with the twisted boundary condition we use the trick [58] proposed by Lüscher and Weisz. To reduce large statistical fluctuation of the TPL coupling constant, as reported in Ref. [63], we measure Polyakov loops at every Monte Carlo sweep and perform a jackknife analysis with large bin size, typically of $O(10^3)$. The simulations are carried out with several lattice sizes ($L/a = 4, 6, 8, 10, 12, 14, 16$) at more than twenty β values in the range $6.2 \leq \beta \leq 16$. We generate 200,000-400,000 sweeps for each parameter set $(\beta, L/a)$.

To investigate the evolution of the renormalized running coupling, we use the step scaling method [53]. Firstly we chose a value of the renormalized coupling $u = g_{\text{TPL}}^2(\beta, a/L)$ at the energy scale $\mu = 1/L$. For each L/a in the set of reference lattice size, we find the value of β which produces a given value of the renormalized coupling, u . Then, we measure the step scaling function on the lattice

$$\Sigma(u, a/L; s) = g_{\text{TPL}}^2(\beta, a/sL) \big|_{g_{\text{TPL}}^2(\beta, a/L) = u}, \quad (3.1)$$

by using tuned value of β for each lattice size sL/a . Here, s is the step-scaling parameter. The step-scaling function in the continuum limit, $\sigma(s, u)$, is obtained by taking the continuum

extrapolation of $\Sigma(u, a/L; s)$:

$$\sigma(s, u) = \lim_{a \rightarrow 0} \Sigma(u, a/L; s) |_{g_{\text{TPL}}^2(\beta, a/L) = u}. \quad (3.2)$$

This step scaling function ($\sigma(s, u)$) corresponds to the renormalized coupling at the scale $\mu = 1/sL$.

Figure 2 shows the β dependence of the coupling constant in TPL scheme at various lattice sizes. The results are fitted at each fixed lattice size to the interpolating function which is similar to the one used in Ref. [8],

$$g_{\text{TPL}}^2(\beta) = \sum_{i=1}^n \frac{A_i}{(\beta - B)^i}, \quad (3.3)$$

where A_i are the fit parameters, and $4 \leq B \leq 5$, $n = 3, 4$ are employed. As reference lattice sizes of the step scaling, we use $L/a = 4, 6, 8, 10$. The step scaling parameter is $s = 1.5$, and we estimate the coupling constant for $L/a = 9, 15$ from interpolations at the fixed β using the above fit results of all the lattice sizes.

We take the continuum limit using a linear function of $(a/L)^2$, because the TPL scheme involves no $O(a/L)$ error. We found that the coupling constant in the TPL scheme exhibits scaling behavior even at the smaller lattice sizes, as shown in Fig.3.

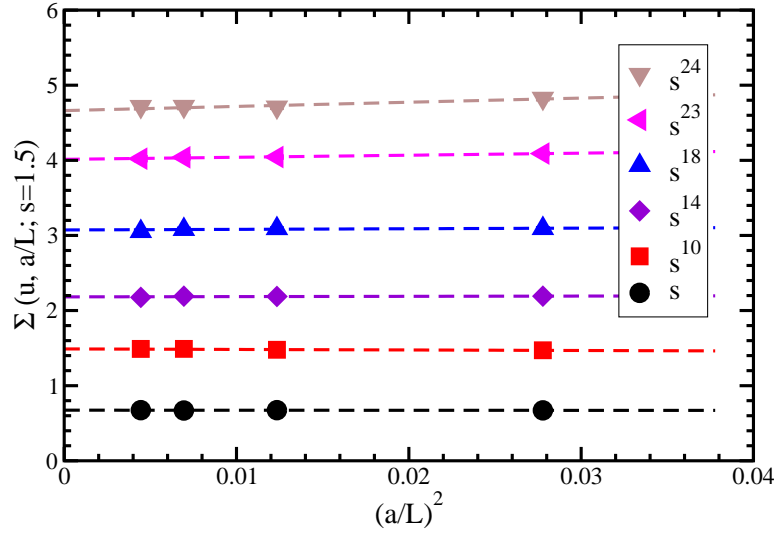


Fig. 3 The continuum extrapolations of g_{TPL}^2 for the scale $L/L_0 = s^n$. The fit function is a linear function of $(a/L)^2$. The data from left to right correspond to $L/a = 15, 12, 9, 6$. The statistical error bars are of the same size of the symbols.

The running of the TPL coupling constant in quenched QCD with 24 steps is shown in Fig.4 together with one- and two-loop perturbative results. The horizontal axis corresponds to the energy scale. All the results are normalized at $L = L_0$ with $g^2(L_0) = 0.65$. The non-perturbative running coupling constant is consistent with one- and two-loop perturbative results in the high energy region ($L_0/L \geq 0.1$). Comparison with the other nonperturbative analyses in SF scheme and Wilson loop scheme are also interesting. The both SF (Fig. 1 in the paper [64]) and Wilson loop (Fig.8 in the paper [65]) running coupling constants show

that similar behavior; faster than one-loop in the nonperturbative region. On the other hand the TPL running is slightly slower than one-loop.

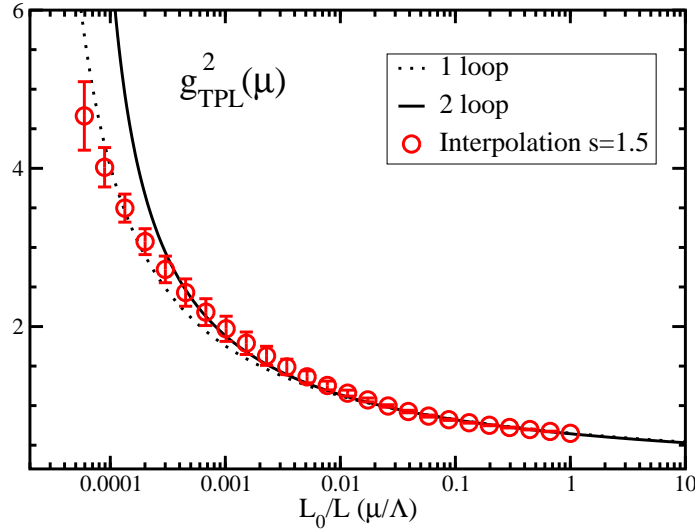


Fig. 4 The running coupling constants in TPL scheme, and in perturbative one-loop and two-loop calculations.

From this quenched test, we conclude that we can control both the the statistical and systematic errors of the TPL coupling constant. Furthermore we find that the TPL coupling constant in quenched QCD has a robust scaling behavior even in a small lattice size, which was also observed in the previous quenched SU(2) calculations [56, 63].

4. Vacuum structure of the $N_f = 12$ theory with twisted boundary condition

Now, we would like to consider the SU(3) theory coupled to $N_f = 12$ fundamental fermions. In this section, we discuss the center symmetry of SU(3) gauge group to define the true vacuum in this theory. The generators of the center symmetry of SU(N_c) pure gauge theory are $z = \exp(2\pi i l / N_c)$, where $l = 0, 1, \dots, N_c - 1$. This symmetry is broken by adding fermions to the theory, leading to the existence of a unique vacuum in an SU(3) gauge theory involving massless fermions in the deconfinement phase. We discuss the vacuum structure which is an important to study of the gauge theories in finite volume.

Let us focus on the center symmetry of this theory. Although the Wilson gauge action is invariant under the following transformation for the link variable for each direction,

$$U_\mu(t, \vec{x}) \rightarrow z U_\mu(t, \vec{x}), \quad (4.1)$$

the fermion is not invariant.

At the perturbative one-loop level, the semi-classical free energy for the gauge configuration $\{U\}$ is given as

$$F^{(\text{tree and one-loop})} \equiv S_g(U) + S_g^{\text{one-loop}}[U] - N_f \ln \det[D(U)]. \quad (4.2)$$

With the twisted boundary condition, the flat potential due to the toron contribution is lifted because of the nonzero momenta in twisted directions and the free energy has $3^4 = 81$ -fold

(θ_z, θ_t)	$-\ln \det(D) - S_0$
$(0, 0)$	0
$(0, 1 \text{ or } 2) \text{ or } (1 \text{ or } 2, 0)$	-57.19
$(1 \text{ or } 2, 1 \text{ or } 2)$	-89.56

Table 2 The $\theta_{z,t}$ dependence of semi-classical free energy for 6^4 lattice. We take a reference potential energy $S_0 = -3511.68$ which is the one in $(\theta_z, \theta_t) = (0, 0)$.

degenerate classical minima at $U_\mu = \exp(2\pi i \theta_\mu / 3) \mathbb{I}$, where $\theta_\mu = 0, 1, 2$ for each direction. The Wilson gauge action (S_g) and the one-loop contribution from gauge part ($S_g^{\text{one-loop}}[U]$) respects the Z_3 symmetry, so that we do not consider them in what follows.

Let us consider the fermion determinant. In the momentum space, there are the physical and unphysical momenta ($\hat{k}_\mu = \hat{k}_\mu^{ph} + \hat{k}_\mu^\perp$) in the twisted directions, that also appear in the gauge field momenta (eq. (2.12)). In the case of the fermion field, the color and smell degree of freedom of ψ_α^a in eq.(2.7) can be transferred into the unphysical momentum degrees of freedom: their number is $N_c \times N_s$ ². Here, we replace the momentum as

$$\hat{k}_\mu \rightarrow \hat{k}_\mu^\theta \equiv \hat{k}_\mu + 2\pi i \theta_\mu / 3\hat{L}. \quad (4.3)$$

The Z_3 transformation in eq. (4.1) can be defined on each lattice site independently, so that we can take a typical gauge in which $U_\mu = \exp(2\pi i \theta_\mu / 3\hat{L})$ for whole lattice volume. Then the fermion action in the vacuum $U_\mu = \exp(2\pi i \theta_\mu / 3\hat{L})$ is obtained by the above replacement. The fermion determinant in finite volume \hat{L}^4 is thus

$$-\ln \det[D] = -8 \sum_{\hat{k}} \ln \left(\sum_{\mu} \sin^2(\hat{k}_\mu^\theta) \right). \quad (4.4)$$

In the Table 2, we show the results of the fermion determinant (eq.(4.4)) for $L/a = 6$. We find that the vacuum free energy is independent of $\theta_{x,y}$ and there are three types of vacuum classified with $\theta_{z,t}$. The first one is a “trivial vacuum”, in which vacuum $(\theta_z, \theta_t) = (0, 0)$. This vacuum has 9-fold degeneracies. The value of the free energy is highest among three types of vacuum, so that it will decay to the true vacuum. The second one is a “half-trivial vacuum”, in which one of $\theta_{z,t}$ is 1 or 2 and the other one is $\theta_\mu = 0$. This vacuum has 36-fold degeneracies. The free energy is higher than the one of the third vacuum, so that this vacuum is also unstable. The third one, in which the free energy is lowest, is a “non-trivial vacuum”. Both θ_z and θ_t take 1 or 2, and there are also 36-fold degeneracies. The free energy has minima at this vacuum and in this non-trivial vacuum all classical link variables for z and t directions has a non-trivial phase $U_{z,t} \propto \exp(\pm 2\pi i / 3\hat{L})$. This means that the Polyakov loop for z direction also has a non-trivial phase $\exp(\pm 2\pi i / 3)$.

This classification is hold for generic lattice size, and it turns out that the potential differences between the true non-trivial vacuum and the other vacua become small when the lattice size become large, although the potential barrier must become high. If we change

² In the case of $N_s = n_s \times N_c$, there are n_s flavor fermions whose momentum in the twisted directions have $N_c \times N_c$ unphysical modes

the fermion boundary condition in z and t direction, then the semi-classical free energy has minima at the other vacuum.

5. Simulation setup for the $N_f = 12$ theory

Our numerical simulation is performed in the following setup. The gauge configurations are generated by the Hybrid Monte Carlo algorithm, and we use the Wilson gauge and the naive staggered fermion actions. In Sec. 6, the simulations are carried out with lattice sizes $L/a = 4, 8$ and 12 at several low β and a broad range of ma to study the phase structure in this system. We generate 1,000 – 2,000 trajectories for each parameter set in the case of $L/a = 4$ and 8 , and also generate 500 – 1,000 trajectories for each in the case of $L/a = 12$.

The measurement of the coupling constant in Sec. 7 are carried out with lattice sizes $L/a = 6, 8, 10, 12, 16$ and 20 ³ at around thirty β values in the range $4.0 \leq \beta \leq 100$. To reduce statistical fluctuations, we measure the Polyakov loops at every trajectory and bin the data by taking the autocorrelation into account. Using the jackknife method, typical statistical errors of correlator are 2 – 3%. We also estimate the statistical error within the bootstrap method in the whole analysis in Sec. 7, whose results are consistent with the jackknife analysis.

6. Simulation results: Phase structure of $N_f = 12$ SU(3) theory with the twisted boundary condition

In this section, we investigate the phase structure of the $N_f = 12$ fermion theory on the lattice. Although the main purpose of this paper is to derive the running coupling behavior in the massless $N_f = 12$ theory, in order to fully understand the phase structure we need to understand the phase structure of the whole region of the theory space including the mass parameter. Actually, there are several studies which reported the existence and absence of the bulk phases in the case of $N_f = 12$ staggered fermion system [19, 24]. The paper [24] suggested a shift symmetry broken phase in the case of the improved staggered action, and the paper [19] reported that there is no such phase in the case of the naive staggered action and the shift broken phase comes from the improvement of the staggered fermion action. Furthermore it is suggested that there is the spontaneous chiral symmetry broken phase in the strong coupling limit for $N_f \leq 52$ [20, 66]. In our simulation, we use the naive staggered and introduce the twisted boundary. It is important to show the phase structure in our lattice setup independently. We identify the parameter range to study the TPL coupling constant.

At first the plaquette values on the $\beta - ma$ plane be reported in Sec. 6.1. In Sec. 6.2 we discuss the complex phase of the Polyakov loops and the phase structure of the theory. In Sec. 6.3, the tunneling behavior between the degenerate vacua and whose effect to the TPL coupling constant are discussed.

³ We generated the data with $L/a = 4$ as same as the quenched QCD case, however, we found there is a large discretization effects in the case of $N_f = 12$ [2], and the systematic uncertainty could not be controlled. Then we dropped the data from this analysis.

6.1. Plaquette values on the $\beta - ma$ plane

Let us investigate the plaquette values of the $\beta - ma$ plane. The left panel of figure 5 shows the plaquette values on $(L/a)^4 = 4^4$ lattice in the $\beta - ma$ plane in the range of $0 \leq ma \leq 0.2$. Most of the configurations are thermalized from massive to massless direction except for the small mass region in the $\beta = 3.8$ as we explain later.

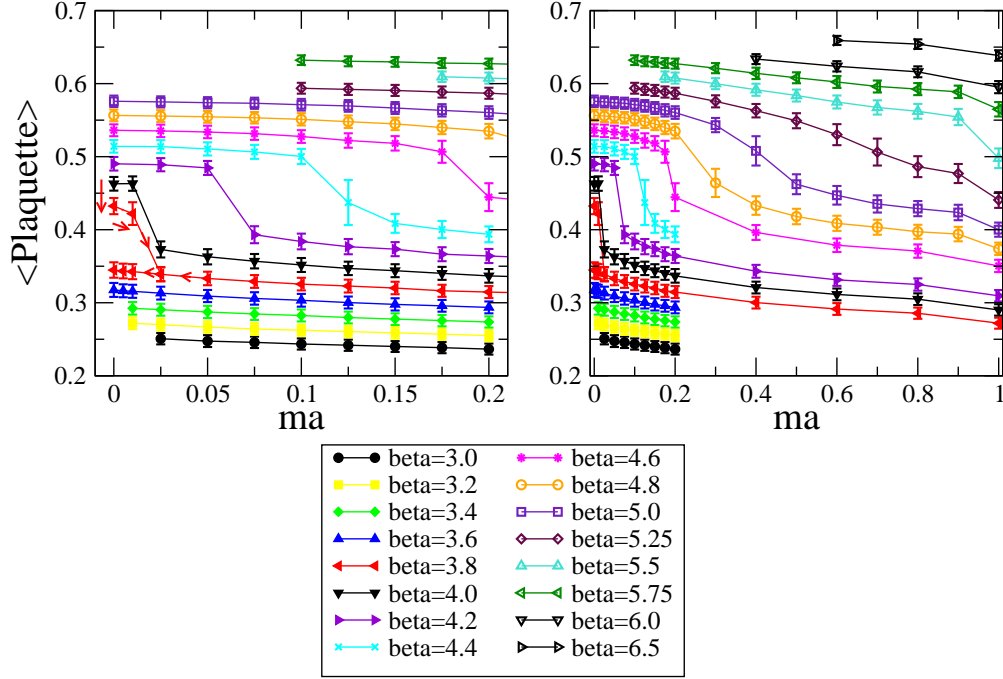


Fig. 5 Plaquette values for several β and ma on $(L/a)^4 = 4^4$ lattice. The data at $ma = 1$ on the right panel denotes the quenched QCD. The small (red) arrows near the massless at $\beta = 3.8$ on the left panel shows the detailed history of the thermalization. The other data are thermalized from massive to massless direction.

First of all, we found there are gaps of the plaquette in the lines of fixed ma . The gap appears between $\beta = 4.8$ and $\beta = 4.6$ for $ma = 0.2$ and in the smaller mass region it happens at the lower β . Near the massless limit the gap exists around $3.6 \leq \beta \leq 4.0$.

The small (red) arrows near the massless at $\beta = 3.8$ on the left panel in Fig. 5 shows the detailed histories of the thermalization. We find that there are two different values in the $0 \leq am \leq 0.0125$ region. The configurations giving larger values of the plaquette at the same ma are thermalized from the massless configuration in $\beta = 4.0$; on the other hand those giving smaller values are obtained from the massive configuration at fixed β . It clearly shows the first order phase transition around this region. At $\beta = 4.0$ and $\beta = 3.6$, there is no dependence on the thermalization process.

We also study the larger mass region. The right panel in Fig. 5 shows the same plot with the left for a broader region of ma . In the quenched limit, we know that there is the first order phase transition. In the figure, we plot the data for the quenched lattice at $ma = 1.0$. The gap seems milder in the larger mass region.

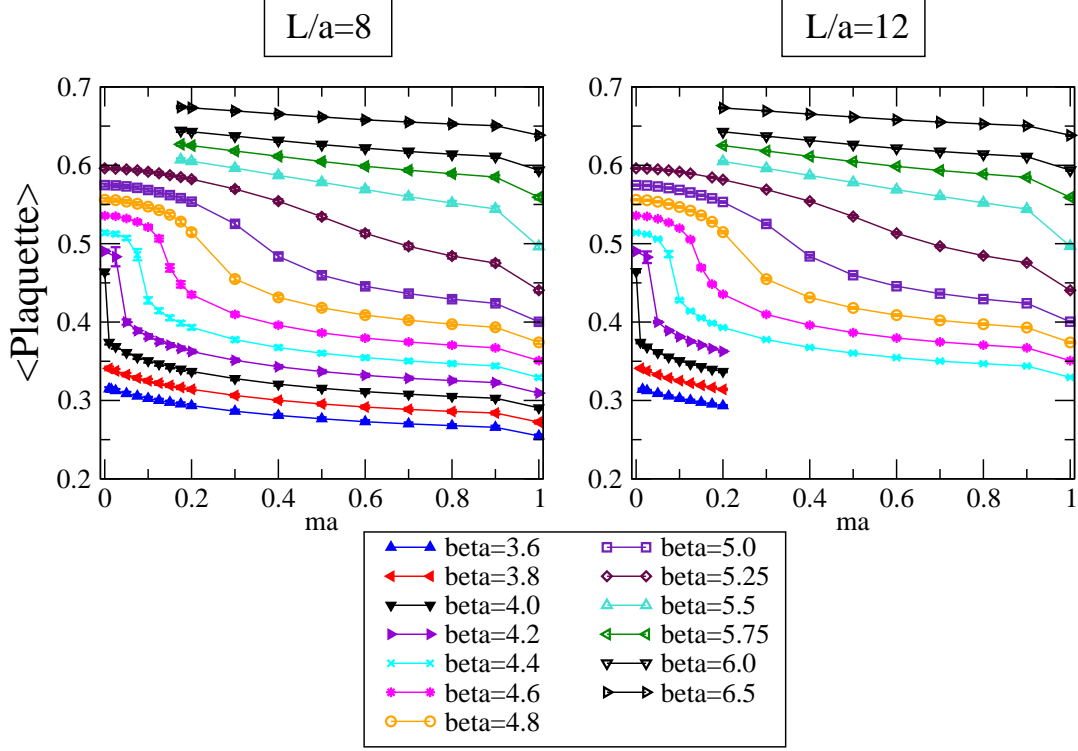


Fig. 6 Plaquette values for several β and ma on $(L/a)^4 = 8^4, 12^4$ lattice. The data at $ma = 1$ denotes quenched QCD. The statistical error is the same size of the symbol.

We also investigate this first order phase transition near the massless region by changing the lattice volume in Fig. 6. There are slight differences between $L/a = 4$ and $L/a = 8$ for the critical value of β , for example at $ma = 0.175$ the data for $\beta = 4.6$ on $(L/a)^4 = 4^4$ is in the upper phase of the gap, but it moves to the lower phase in the case of $(L/a)^4 = 8^4$. The results on $(L/a)^4 = 8^4$ and 12^4 show the similar behavior at least the present interval of β and ma ($\Delta\beta = 0.2, \Delta ma = 0.01 - 0.025$), and there is no clear volume dependence. The massless simulation at $\beta = 3.8$ needs extremely finer molecular-dynamics time step size than $\Delta\tau = 0.002$ ($\tau = 1$ is 1 trajectory), and then practically we could not generate the data. The position of β where the simulation becomes quite costly is the same in the both $L/a = 8$ and $L/a = 12$. This supports the understanding that there is a bulk phase transition.

6.2. Polyakov loop

Next, let us investigate the Polyakov loop. Now, there are dynamical fermions and the center symmetry is broken explicitly, and thus there is no clear order parameter for the deconfinement phase transition. However, here we use the word “deconfinement” phase as where a magnitude of Polyakov loop is clearly nonzero on the lattice. At first, we show the complex phase of Polyakov loop.

In the case of the quenched QCD, there is Z_3 symmetry, and there is tunneling between them on finite lattices. In the case of $N_f = 12$ massless theory with the twisted boundary

condition, the Z_3 symmetry is broken and the true vacua is the one that the Polyakov loops in the untwisted directions have the nontrivial phase as explained in Sec. 4.

We present the scatter plots of the typical Polyakov loops for the massless theory in the twisted and untwisted directions in the left and right panels in Fig. 7 respectively. The

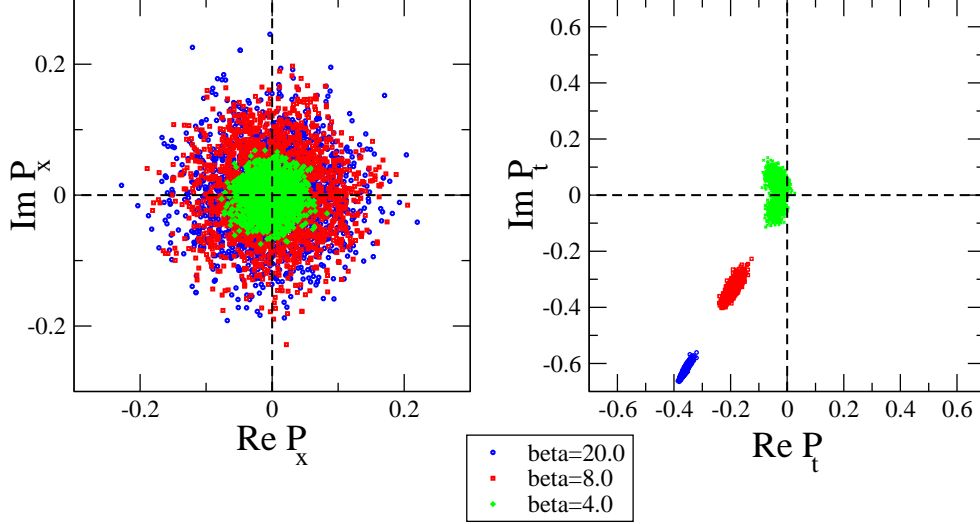


Fig. 7 Scatter plots of the Polyakov loop in the twisted ($\mu = x$) and the untwisted ($\mu = t$) directions in the complex plane. The lattice size is 6^4 and circle(blue), square(red) and cross(green) symbols denote $\beta = 20.0, 8.0, 4.0$ respectively.

Polyakov loop in the twisted direction clearly shows the independence of the complex phase. That is consistent with the tree level analysis, in which $\langle P_x \rangle = 0$ because of the traceless twist matrix in the eq.(2.8). This does not depend on the value of β and it is not related to whether the system is in the confinement or in the deconfinement phase. On the other hand, the Polyakov loop expectation value in the untwisted direction has clearly the nontrivial phase $\exp(\pm 2\pi i/3)$ in the high β region. In $\beta = 4.0$ the tunneling occurs between the two phases, but apart from the tunneling the values of the phase are close to $\exp(\pm 2\pi i/3)$. Thus, we confirm that the Polyakov loops in both the directions are consistent with the results of from the semi-classical analysis in Sec. 4 even in the strong coupling region. The effect of the tunneling on the TPL coupling will be discussed in the next subsection.

From these scatter plots, the real part of the Polyakov loop in t -direction is a negative nonzero value in the deconfinement phase because the nontrivial phase vacua are chosen as shown in Sec. 3. The left two panels in Fig. 8 shows the real part of the Polyakov loop in t -direction at several fixed ma in the case of $L/a = 4$. The Polyakov loop in the high β region clearly deviates with zero for all ma , which implies that the system stays in the deconfinement phase. On the other hand, at the low β region that is consistent with zero and the theory shows the confinement behavior. In the case of massless $L/a = 4$ we find a gap at the $\beta = 3.8$, which is at the same position for the plaquette study. For β smaller than the gap position, the real part of the Polyakov loop is not consistent with zero, but it goes to zero continuously. In the finite mass region, there is a weak jump, and the gap become

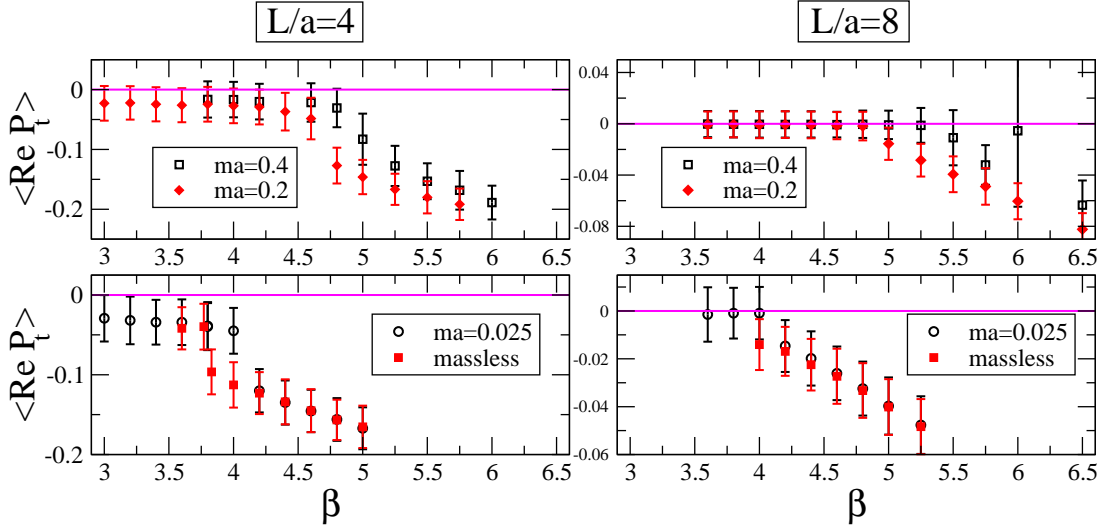


Fig. 8 Left panel: real part of the Polyakov loop in t direction in the case of $(L/a)^4 = 4^4$. Clearly there is a gap for each ma . In the case of the massless, the measured data at $\beta = 3.8$ are shifted; the one of them shows at $\beta = 3.77$ which corresponds to the configurations at $\beta = 3.8, ma = 0$ whose plaquette value is the larger one in Fig. 5. The other shows at $\beta = 3.83$ which corresponds to the configurations at the same β and ma whose plaquette value is the smaller one in Fig. 5. Right panel: the same plot in the case of $(L/a)^4 = 8^4$.

larger in the smaller mass region. The value of the critical β in which the data shows the jump is the same with the plaquette study.

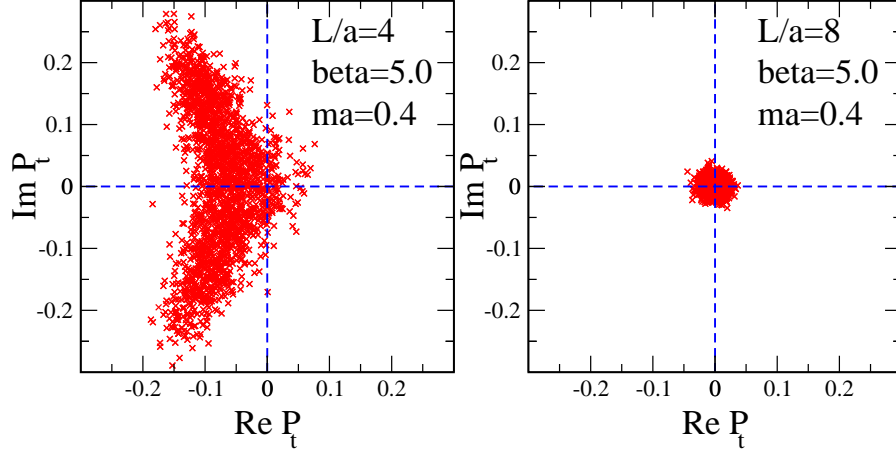


Fig. 9 Left panel: real part of the Polyakov loop in t direction in the case of $\beta = 5.0, ma = 0.4, (L/a)^4 = 4^4$. Right panel: the same plot in the case of the same β and ma on $(L/a)^4 = 8^4$.

Let us study the lattice size dependence. We show the real part of the Polyakov loop in the case of $L/a = 8$ in the right panels in Fig. 8. There is no clear jump in the case of $L/a = 8$, but the real part of the Polyakov loop approach to the zero in the low β region. Note that at large mass region, for example $\beta = 6.0, ma = 0.4$, we can find that the theory

is in the deconfinement phase from the scatter plot of the Polyakov loop on the complex plane, although the real part of the Polyakov loop is consistent with zero. At the parameter the fermion mass is too heavy, and then there is the tunneling between Z_3 vacua as in the quenched case. In this analysis, the number of trajectories is the same for each parameter set at the fixed mass and then we can naively find such a fake $\text{Re } P_t = 0$ data from the size of error bars and can confirm it by the scatter plot.

In the top panels of Figs. 8, the theory with $ma = 0.4, L/a = 8$ is in the confinement phase for $\beta \leq 5.0$, while in the case of $L/a = 4$ the theory is in the deconfinement phase for $4.8 \leq \beta$. Actually, figure 9 is the scatter plots showing a clear difference. On the other hand, $ma = 0.025$ shows the transition between $\beta = 4.2$ and $\beta = 4.0$, it is the same position in the case of $L/a = 4$. At least the current interval of β and ma , we cannot find the volume dependence in the small mass region. The data for $ma = 0.4$ and 0.2 show the volume dependence, and then it seems to be crossover for both the bulk and the finite volume phase transitions. In the case of the (nearly) massless fermion, the transition becomes bulk, and the theory with the massless fermion lies in the deconfinement phase for $\beta \geq 4.0$. The value of the critical β is the same with the one of the gap of the plaquette. In Figs. 5 and 6, the phase for β larger than the gap position can be identified as the deconfinement phase and that for β smaller than the gap position must be the confinement phase. Furthermore, in the case of $L/a = 12$, we cannot find clear nonzero value of the Polyakov loop in the whole region since the current preliminary statistics is small and the Polyakov loop in the low β region is noisy. The gap of the plaquette and the confinement/deconfinement phase transition seems to occur simultaneously, and there is no difference between $L/a = 8$ and $L/a = 12$ of the plaquette behavior. At least we found that the position of β where the simulation becomes quite heavy is the same in the case of $L/a = 8$.

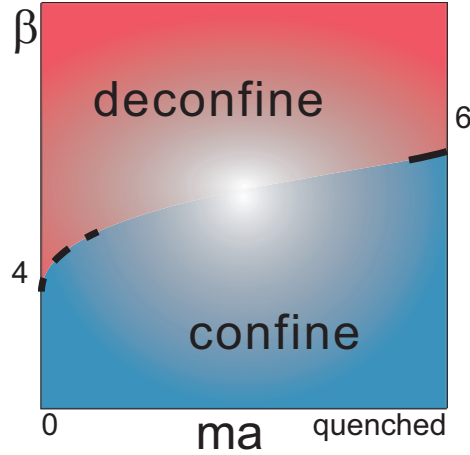


Fig. 10 The phase structure of $N_f = 12$ $SU(3)$ theory with naive staggered fermion. The dashed line denotes bulk phase transition and the solid line denotes the finite volume phase transition.

The summary of the phase structure and the available region of the TPL coupling for the quenched and the massless $N_f = 12$ QCD is the following. Figure 10 is a sketch of the phase structure for the naive staggered $N_f = 12$ $SU(3)$ theory. In the case of the quenched

QCD, the correlation length becomes shorter in the lower β region, and there is the finite volume phase transition where the theory goes to the confinement phase. In the case of the massless $N_f = 12$ SU(3) theory, there is the similar behavior while the transition seems the bulk one at $\beta < 4.0$. In both cases, the boundary condition is negligible in the confinement phase where the correlation length of the Polyakov loop is smaller than the lattice extent, and then the TPL coupling becomes the constant. In the study on the running coupling constant in TPL scheme, we should focus on only the deconfinement phase on the lattice.

Finally, we show that our massless configurations to study the running coupling constant live in the deconfinement phase (although it might be trivial since the transition seems to be the bulk and we concentrate on the parameter region within $\beta \geq 4.0$). Figure 11 shows the

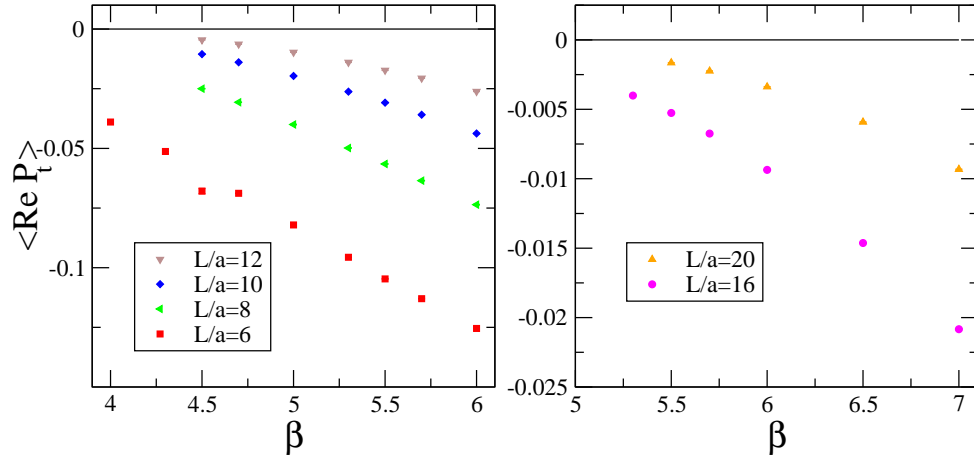


Fig. 11 Real part of the Polyakov loop in the untwisted ($\mu = t$) direction as a function of the lattice size at $\beta = 6.0$. The statistical error bars are the same size of the symbols.

real part of the Polyakov loop for the low β region for each lattice size. All data points clearly show that $\text{Re } P_t$ take the non-zero values. This observation indicates that all configurations used in our analysis in Sec. 7 are in the deconfinement phase.

6.3. Tunneling behavior between true vacua

During the Monte Carlo simulation, the tunneling can occur between the two degenerate vacua in each untwisted direction independently. The tunneling behavior is a lattice artifact, since the potential barrier between the vacua becomes finite due to the finite lattice spacing. In this subsection, we would like to consider how the TPL coupling is disturbed by the tunneling behavior.

The tunneling is expected to occur more frequently in the strong coupling region. We observe some tunnelings in low β region, although the number of the tunneling is quite small, and decreases as β increases. For $L/a = 6$ we observe the tunneling 7 times per 6,000 trajectories in the stronger coupling region, $\beta = 4.0$, and almost no tunneling, 3 times per 90,000 trajectories, at $\beta = 6.0$.

A typical example of the tunneling is shown in figure 12. The left panel denotes the history of the imaginary part of the Polyakov loop in the untwisted direction at $\beta = 4.0$ on $L/a = 6$. In the figure the sign of the imaginary part is flipped in the 1,400 – 1,600th trajectories.

Let us see the effects of the tunneling on the TPL coupling defined by the ratio of the Polyakov loop correlators in eq.(2.9). The right panels in Fig. 12 present the histories of the

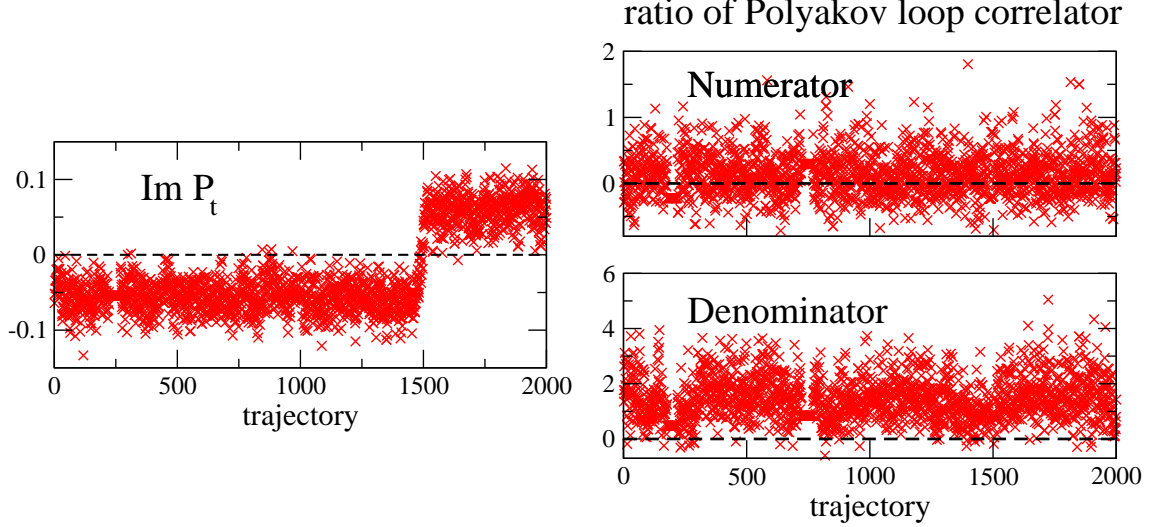


Fig. 12 Left panel: History of the imaginary part of the Polyakov loop in untwisted ($\mu = t$) direction at $\beta = 4.0$ in $L/a = 6$. Right panels: Histories of the numerator and denominator of the TPL coupling eq.(2.9) in the same trajectories of the left.

numerator and denominator of the TPL coupling obtained from the same configuration as in the left panel. During the tunneling, *i.e.*, the 1,400 – 1,600th trajectories, both the results seem not to exceed the range of each statistical fluctuation. This means that the tunneling does not significantly affect the result of the TPL coupling calculated by the ratio of the expectation values for the numerator and denominator.

Therefore we conclude that effects of the tunneling on the TPL coupling is negligible at least in our calculation due to the rare occurrence of the tunneling and the large statistical fluctuation of the Polyakov loop correlators.

7. Simulation results: Step scaling function for $N_f = 12$ SU(3) gauge theory

In this section, the step scaling function in the case of $N_f = 12$ flavor are derived. We focus on the growth rate of the step scaling function as a function of the input renormalized coupling. This quantity is a suitable for showing the precise behavior of the running coupling constant, and becomes unity when there is a zero in the beta function. At first, we will discuss the global behavior of the growth rate from the perturbative to the IR region in Sec. 7.1. The nonperturbative running behavior shows the signal of the conformal fixed point in the IR region. Then, we focus on the low energy region only and derive again the step scaling function by using the data only in the strong coupling region in Sec. 7.2. We discuss the stability of the IR fixed point by considering several systematic uncertainties and derive the universal quantity for the exponent of the beta function around the IRFP in Sec. 7.3.

7.1. The global behavior of the step scaling function

Before explaining the simulation details, we address the guiding principles of our simulation to show the global behavior of the running coupling. We use the step scaling method as same as the quenched case. For each L/a we use the interpolation in β . Since the choice of the interpolation function can affect the step scaling function, we should take care of the following two points:

- (1) We generate data in a broad range of β , with intervals that the renormalized coupling constant (g_R^2) grows almost constantly in each interval. Thus the interval of β is large in high β region while small in the low β region. Each data have a similar accuracy (2 – 3%).
- (2) We employ fit functions for β interpolation which reproduce the tree level result $g_R^2 \simeq g_0^2$ on each lattice size in extremely high β region.

These guiding principles ensures the stability of our fit results under the change of fit functions and the number of data. Point 1 is needed to ensure that the fit functions do not favor any special region of the data when we interpolate our data in β or extrapolate to in $(a/L)^2$. To satisfy this point is very important to search for the IRFP by using the numerical simulations, since finally the interpolation function of the data decides the step scaling function. We discuss the dependence of the data set for the global fit analysis in Appendix D, in the case where the data are concentrated in some particular region. The result in Appendix D do not have a nice agreement with the perturbative result and in the IR region the position of the IRFP strongly depends on the fit range. Point 2 is needed to reduce the effect of statistical fluctuation in high β region. In high energy region, since the coupling runs very slowly, we need extreme high statistics to reproduce the perturbative result only by the numerical data. The assumption of the point 2 makes the result stable in high energy region.

In Fig.13, we show our simulation results for the renormalized coupling in TPL scheme as a function of $1/\beta$ for each L/a . The raw data are given in Tabs. A1 and A2 in Appendix A. The left panel in the Fig. 13 shows a global behavior of the TPL coupling. We can see the high energy behavior seems to be almost linear in $1/\beta$ as expected from the perturbation theory. The right panel focuses on the low β region. In the low β region for $L/a = 6$ the TPL coupling has a maximum at $\beta = 4.3$. In the contrast to the Schrödinger functional scheme [8], there is no inversion of the lattice size dependence at fixed β . We consider that this difference comes from the lattice artifact which depends on the renormalization scheme. To remove the effect, the careful continuum extrapolation is necessary.

For β -interpolation, we use the following form of fitting function:

$$g_{\text{TPL}}^2(\beta, a/L) = 6/\beta + \sum_{i=1}^N C_i(a/L)/\beta^{i+1}, \quad (7.1)$$

where $C_i(a/L)$ are the fitting parameters and N is the degree of the polynomial. Here, $N = 3 - 5$ are employed. We drop $\beta = 4.0, L/a = 6$ from the fit to avoid the double solutions when we solve the β values to reproduce the input renormalized coupling (u). This limits us to study the step scaling in the range $u \leq 2.94$, where $u = 2.94$ is the renormalized coupling constant g_{TPL}^2 at $\beta = 4.3, L/a = 6$, in this lattice set up.

To investigate the evolution of the renormalized running coupling, we use the step scaling method as explained in Sec. 3.2. In this study, we take $s = 1.5$, and denote $\sigma(u) \equiv \sigma(s=1.5, u)$ in the rest of this paper for simplicity. The set of small lattice is taken to be $L/a = 6, 8, 10, 12$,

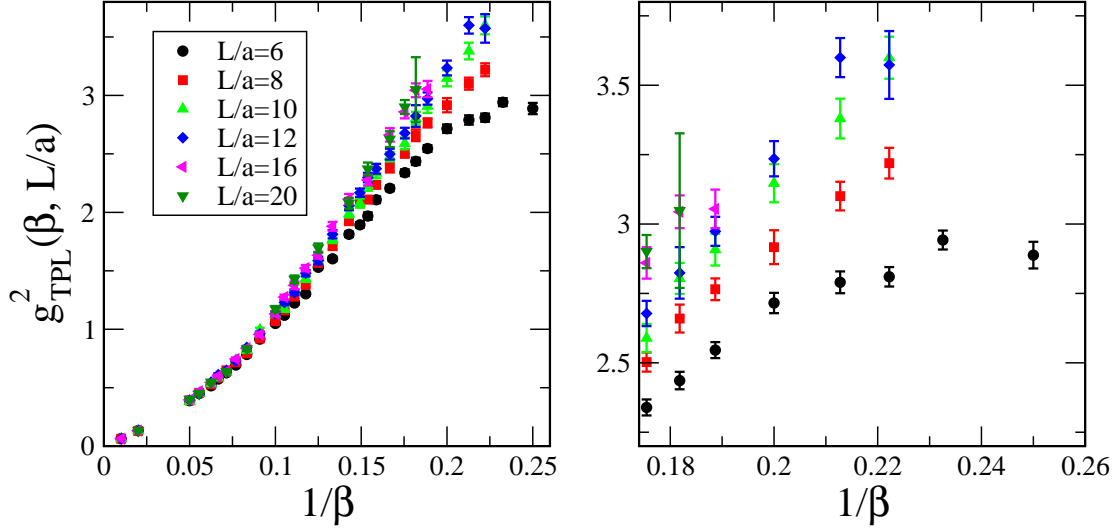


Fig. 13 TPL coupling for each β and L/a . Left panel: Plots for the global region of β . Right panel: Plots only for the low β region.

therefore, we need values of g_{TPL}^2 for $L/a = 9, 12, 15, 18$ to take the continuum limit in Eq. (3.2). For $L/a = 9, 15$ and 18 , we estimate values of g_{TPL}^2 for a given β by the linear interpolation in (a/L) with using the data on the lattices $L/a = \{8, 10\}$, $\{12, 16\}$ and $\{16, 20\}$, respectively. To estimate the systematic error of this interpolations, we also performed the linear interpolation in $(a/L)^2$, and found that the difference between a/L and $(a/L)^2$ interpolations is negligible. Furthermore, we will also show the $s = 2$ step scaling in which there is no interpolation of L/a , and the difference of the result should give an indirect estimation of the systematic error from the interpolation in L/a .

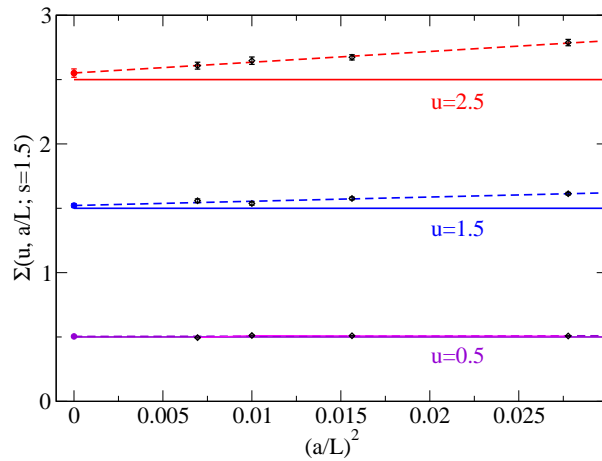


Fig. 14 Continuum extrapolation for the case of input coupling $u = 0.5, 1.5$ and 2.5 from the bottom to top respectively. Each solid line denotes the input renormalized coupling u , and the dashed line with the corresponding color denotes the linear extrapolation function of $(a/L)^2$.

In Fig. 14, we show the examples of the continuum extrapolation for obtaining $\sigma(u)$ in the weak, intermediate and strong coupling regions. We determine the central value of $\sigma(u)$ by the linear extrapolation in $(a/L)^2$ with four points; $L/a = 6, 8, 10, 12 \rightarrow 9, 12, 15, 18$ since the leading order of the discretization error comes from $O(a^2)$ in this scheme. Note that, in the strong coupling region, each lattice data $\Sigma(u, a/L; s = 1.5)$ (black data point) is quite larger than u , however, at the continuum limit, $\sigma(u)$ gets close to u . This indicates that it is very important to take the continuum limit carefully in this kind of analysis. We explain the reason why this continuum extrapolation is chosen as the best in this analysis in Appendix E. We also discuss the taste breaking in the continuum limit in Appendix F.

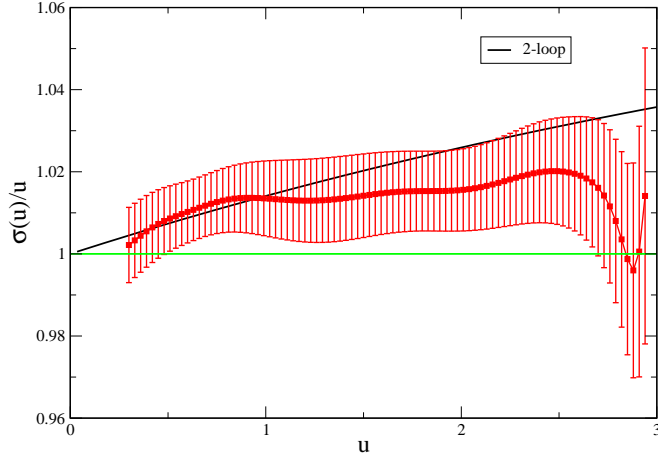


Fig. 15 The growth rate $\sigma(u)/u$ as a function of u with statistical error. Two-loop perturbative value (black line) is also plotted for comparison. The horizontal (green) line denotes unity line, where the beta function is consistent with zero.

Now, we obtain the step scaling function explained above in a wide range of u . Figure 15 shows the growth rate of the renormalized coupling ($\sigma(u)/u$) as a function of u with statistical error which is estimated by jackknife method. We also carried out the bootstrap analysis independently, and found that the results are consistent with this jackknife analysis.

We found two things from this plot. The first one is that the result is consistent with perturbation theory in the weak coupling regime. The TPL coupling coupling with this lattice set up works promising under this analysis method. The other one is the central value of $\sigma(u)/u$ becomes unity around $u = 2.7$, demonstrating the signal of a fixed point. This is the first zero of the beta function from the asymptotically free regime. It suggests the existence of an *infrared* fixed point around the region. Unfortunately, the upper values of the error bars do not cross the line $\sigma(u)/u = 1$. This means that we cannot exclude the possibility for the coupling constant to continue growing within the error bar. We will investigate this quantity again by focusing only the strong coupling region and adding the data. Furthermore, will give an estimation of the systematic error of the fixed point coupling in the next subsection.

7.2. Low energy behavior and stability of the IR fixed point

In the previous subsection, we found a signal of the IRFP around $u = 2.7$ from global fit of the data. Now we focus on the strong coupling region and will determine the fixed point

L/a	β range	# of the data	L/a	β range	# of the data
6	$4.3 \leq \beta \leq 7.0$	17	9	$4.5 \leq \beta \leq 7.0$	17
8	$4.5 \leq \beta \leq 8.0$	27	15	$5.3 \leq \beta \leq 8.0$	16
10	$4.5 \leq \beta \leq 8.0$	27	18	$5.5 \leq \beta \leq 9.0$	7
12	$4.5 \leq \beta \leq 8.0$	21			

Table 3 The fit range of the local fit analysis for each lattice size. The data $L = 9, 15$ and 18 are obtained by the L/a interpolation at the fixed β value as explained in Sec. 7.1.

coupling and the related universal quantity. In this subsection, we take a narrow β range in which β -dependence of g_{TPL}^2 can be approximated by linear or quadratic functions of β . We add more data, which is a part of the data shown in Appendix B, to obtain the precise result and discuss the systematic uncertainties of the IRFP.

Practically, we will carry out the step scaling again with the data only in low β region $u \geq 2.0$. This region roughly corresponds to the range $\beta \leq 7.0$. We choose the fit range for each lattice size as shown in Table 3. The fitting function is chosen as a simple unconstraint polynomial function:

$$g_{\text{TPL}}^2(\beta, a/L) = \sum_{i=0}^{N-1} \tilde{C}_i(a/L)/\beta^i, \quad (7.2)$$

where N is the degree of the polynomial and here we take $N = 3$ for $L/a = 6, 8$ and $N = 2$ for the other lattice size. We derived the step scaling function by using the same procedure

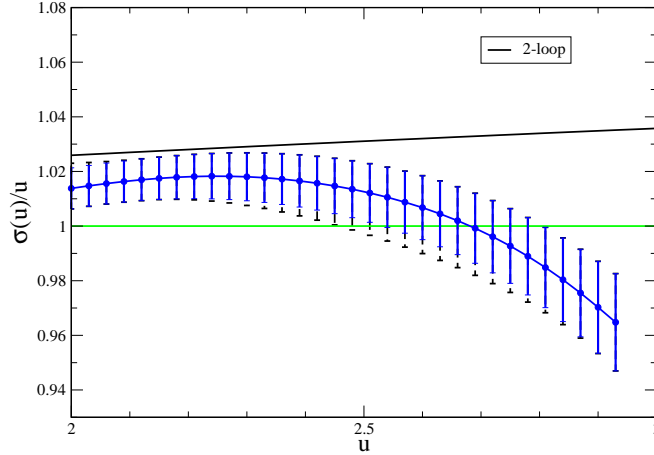


Fig. 16 The local fit result for the growth rate of the TPL coupling. The solid (blue) error bar denotes the statistical error and the dot (black) error includes the systematic error. Two-loop perturbative value (black line) is also plotted for comparison. The horizontal (green) line denotes unity line, where the beta function is consistent with zero.

with the pervious subsection. The growth rate of the step scaling function is shown in Fig. 16. As a central analysis with solid blue error bar, we take the four point linear extrapolation in $(a/L)^2$ with statistical error estimated by the jackknife method. The dot (black) error bar includes the systematic error, we will discuss it soon later. This local fit result clearly crosses the line $\sigma(u)/u = 1$, which shows the existence of the IRFP.

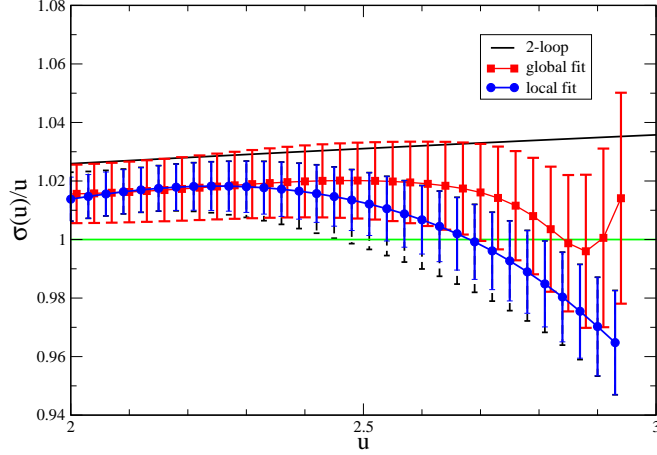


Fig. 17 The comparison of the results with the global fit and those with the local fit. Two-loop perturbative value (black line) is also plotted for comparison. The horizontal (green) line denotes unity line, where the beta function is consistent with zero.

Figure 17 shows the comparison between the local fit result with the global fit result. These two central value are consistent with each other within $1\text{-}\sigma$, despite the change of the data set, the fit range and the fitting function. The results strongly consolidates the existence of the stable fixed point around $u = 2.7$. The error bar for the local fit analysis is smaller since owing to the additional precise data. We also report the data sets dependence and the fit range dependence independently in Appendix C.

Now, we would like to estimate the systematic error in our analysis. There are two possible dominant sources of the systematic error. One is from the choice of the fit range for the β -interpolation (Eq. (7.2)). As shown in Fig. 17, there is a small difference between the global fit and the local fit in Table 3, and we also investigate the further narrow range of the β . Even if we take only the data of $\beta \leq 7.0$ for all lattice size, the fitting function does not show a large difference. We can conclude the systematic error from the choice of the fit range is small in this analysis (see Fig. C1 in Appendix C).

The other dominant systematic error comes from the continuum extrapolation. In Fig. 18, we show the comparisons of several types of continuum extrapolation for $u = 2.0, 2.686$ and 2.85 . As the central value, we take the linear extrapolation in $(a/L)^2$ for $L/a = 6, 8, 10, 12 \rightarrow 9, 12, 15, 18$. We estimate the systematic error by taking the difference between the central value and the result from linear extrapolation without the data on the coarsest lattice $L/a = 6$. Furthermore we compare the central value with the quadratic extrapolation with all the data at four L/a . Figure 18 shows the TPL renormalized coupling has a small systematic error in the strong coupling region, and all the values in the continuum limit agree within $1\text{-}\sigma$ statistical errors. The total error in Fig. 16 is estimated by adding the difference between the continuum extrapolations as a systematic error to the statistical error in quadrature. We conclude that the existence of the IRFP is stable in this analysis.

Finally the renormalized coupling at the IRPF is

$$u^* = 2.69 \pm 0.14 (\text{stat.})_{-0.16} (\text{syst.}). \quad (7.3)$$

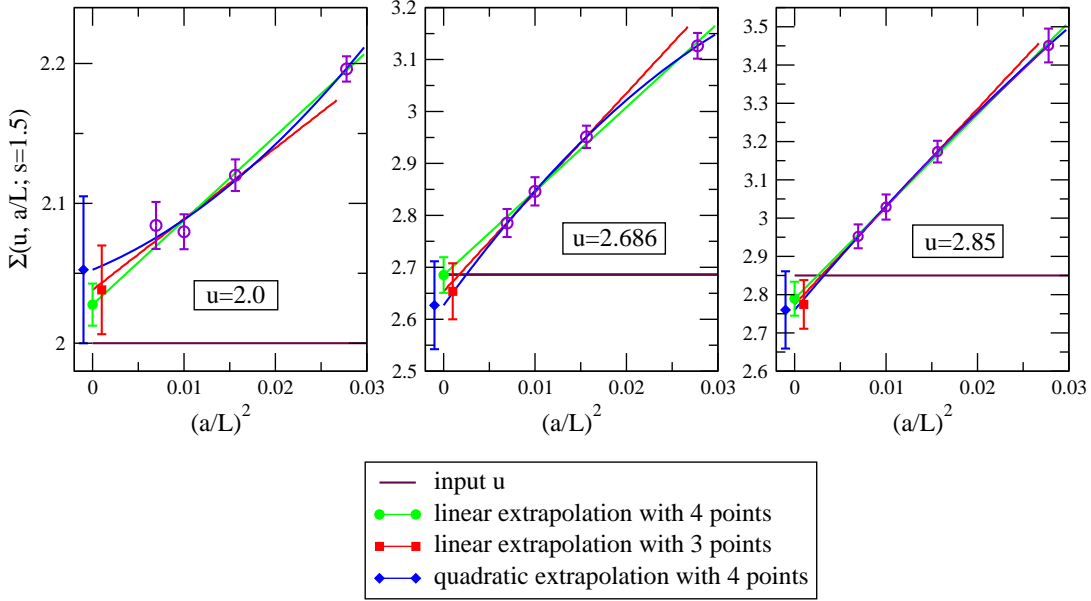


Fig. 18 Continuum extrapolation for the case of input coupling $u = 2.0$, 2.686 and 2.85 . Each green line and the blue curve denote the 4 points linear and quadratic extrapolation functions of $O(a^2)$ respectively. The red line show the linear extrapolation function of $O(a^2)$ for 3 data points without the coarsest lattice data. In the case of $u = 2.0$, the step scaling function is larger than the input value, however, it becomes consistent with u at $u = 2.686$ and for the larger u it is smaller than the input renormalized coupling constant.

Here, the jackknife error of the running coupling is used as a statistical error and we estimated the systematic error coming from the continuum extrapolation. The corresponding β value for each lattice size at $u^* = 2.69$ can be calculated from the β interpolation function in Eq. (7.1): $(\beta, L/a) = (4.91, 6)$, $(5.41, 8)$, $(5.65, 10)$, $(5.79, 12)$, $(5.91, 16)$, $(5.94, 18)$, $(5.94, 20)$. These are the parameter sets which reproduce conformal physics after taking the continuum limit.

In addition, we mention the numerical stability of our results. For this purpose, we perform another step-scaling analysis based on $s = 2$ with $L/a = 6, 8, 10 \rightarrow 12, 16, 20$. The continuum limit is taken by linearly extrapolating three points in $(a/L)^2$. The explicit figure of the growth rate of the renormalized coupling is shown in Fig. C1 in Appendix C. We find that the running behavior in $s = 2$ step scaling is also consistent with that in the case of $s = 1.5$, and the IRFP is found at $u^* = 2.49 \pm 0.19$ (stat.). This is consolidating the existence of the IRFP in this theory.

7.3. Critical exponent

Finally we will derive the critical exponent around the IRFP. In this theory, we have one irrelevant parameter, which is the renormalized coupling constant, around the nontrivial fixed point. The value of the renormalized coupling at the fixed point depends on the renormalization scheme. If we denote the scheme transformation from one renormalization scheme u_1 to the other one $u_2 = F(u_1)$, then in the perturbative region, the function $F(u_1)$ can be

expanded as a polynomial function. The beta function for the renormalized coupling is universal up to two-loop order, however, the nonperturbatively the one for u_2 scheme is related with the other one as follows:

$$\beta(u_2) = \frac{\partial F(u_1)}{\partial u_1} \beta(u_1). \quad (7.4)$$

In the vicinity of the IRFP, the beta function can be approximated by

$$\beta(u) \simeq -\gamma_g^*(u^* - u) + \mathcal{O}((u^* - u)^2). \quad (7.5)$$

Although the value of renormalized coupling at the IRFP is scheme dependent, we can easily find the coefficient γ_g^* around the point is the scheme independent quantity using eq. (7.4).

Now, we compute γ_g^* from the slope of $\sigma(u)/u$ against u , and obtain $s^{-\gamma_g^*} = 0.79 \pm 0.11(\text{stat.})$ in the central analysis in the Fig. 16. This leads to

$$\gamma_g^* = 0.57_{-0.31}^{+0.35}(\text{stat.}) - 0.16(\text{syst.}), \quad (7.6)$$

where the first error is statistical error using the jackknife method and the second one is the systematic error from the continuum extrapolation estimated by the comparison to the 3 point linear continuum extrapolation. The value of γ_g^* is sensitive to the variation of the slope, which causes rather large statistical error. For the $s = 2$ step scaling, the critical exponent of the beta function can be derived $\gamma_g^* = 0.31_{-0.18}^{+0.21}(\text{stat.})$. This is also consistent with our main results with $s = 1.5$.

Our result is consistent with $\gamma_g^{*2\text{-loop}} \sim 0.36$ and $\gamma_g^{*4\text{-loop}(\overline{\text{MS}})} \sim 0.28$ as estimated using 2-loop and 4-loop ($\overline{\text{MS}}$ scheme) perturbation theory [51, 67, 68]. The result in the SF scheme is $\gamma_g^{*SF} = 0.13 \pm 0.03$ [8]. Our result provided a value larger than that in the SF scheme. We can conclude that both results are almost consistent with each other since the discrepancy of γ_g^* is slight larger than $1\text{-}\sigma$.

Another scheme independent quantity which is interesting to observe is the mass anomalous dimension near the IRFP. That is the critical exponent for the relevant operator around the IRFP. We will report it in a forthcoming paper [69].

8. Summary

We gave the explicit definition of the TPL renormalized coupling for SU(3) gauge theory and showed the running coupling constant in the case of quenched QCD and $N_f = 12$ theories. The definition is the extension of the SU(2) gauge theory, and we provided the perturbative calculation to define the coefficient in the case of SU(3).

As a feasibility test for the SU(3) gauge theory, firstly we show the TPL running coupling constant in the case of quenched QCD. In the theory, there is confinement/deconfinement phase transition because of the finite volume effect and we study the behavior of the TPL renormalized coupling constant in the both phases. The TPL coupling have the remarkable property, that in the extremely low energy limit the coupling constant approaches to the constant ($g_{\text{TPL}}^2 \sim 32$ in the case of SU(3) gauge theory), when the theory is in the confinement phase. From this analysis, the TPL coupling is found to be useful only in the deconfinement phase, so that we should take care of the phase in the parameter spaces. The running coupling constant is consistent with the perturbative result in high energy region, and it runs more slowly than that in the 1-loop perturbation in the low energy region. The running behavior is scheme dependent and is different from SF and Wilson loop schemes.

In the case of the theory coupled with fundamental fermions, we have to pay the attention of the vacuum structure. We discussed the vacuum structure and the center symmetry breaking in our simulation setup using the semi-classical analysis, and generated the configurations in the true vacua. The vacuum structure depends on the boundary condition of the fermions, in the case of our definition, the configurations whose Polyakov loop in the untwisted direction has the nontrivial phase shows the minimum of the potential.

Furthermore, we study the phase structure for $N_f = 12$ massive and massless fermion theories. There is a bulk phase transition near the massless region in $\beta < 4.0$. In such phase, the TPL coupling is not available since the theory shows the confinement behavior.

Finally, we have found a solid evidence for the existence of an IRFP in $SU(3)$ gauge theory with 12 massless Dirac fermions in the fundamental representation by using the TPL scheme. The coupling constant at the IRFP is $g_{\text{TPL}}^{*2} \sim 2.69$. The stability of the fixed point is discussed, and we can conclude there is the IRFP after the systematic uncertainties are included.

Acknowledgements and Comments

This basic strategy of the paper was shown in the letter paper [3], which is already withdrawn from the arXiv. Before the letter paper [3] would be published, the collaboration was reset when a part of members released the paper [59] independently, since there was scientific conflicts concerning with the analysis method and the quality of the full paper. This paper includes the further updated data after the collaboration was reset, and the differences of the analysis method are discussed in Appendix D and E.

Some readers could not understand the reason why there are two kinds of data sets in Appendix A and B. Actually, we have not obtained the raw data of the Polyakov loop and configurations in the Appendix B since some members have not send them for more than five months after the collaboration reset while they agreed with sharing the data. Consequently, the analysis of Fig.11 and Appendix F have been done with only the data in Appendix A. Furthermore, as we explained the data sets in Appendix B is strongly prejudiced for a specific region, and that is not suitable to study the global fit analysis.

We would like to thank all ex-collaborators in the proceedings [1, 2] and the letter paper[3] for the discussions. In particular, T. Onogi and T. Yamazaki gave an original idea for the TPL scheme and several important suggestions and comments. The PHB code for the quenched QCD in the Sec. 3.2 was developed by T. Yamazaki. The HMC codes were developed by H. Matsufuru and E. Shintani for several supercomputers, and T. Aoyama and K. Ogawa also gave an effort to developing the GPU code. A part of configuration generations had been done by M. Kurachi, H. Matsufuru, K. Ogawa, H. Ohki, T. Onogi, E. Shintani and T. Yamazaki. We would like to thank these people for the collaboration and would like to address that the original members of this project were T. Onogi, M. Kurachi and E. I. and the collaboration started when we were in YITP, Kyoto.

We also appreciate G. Fleming, P. de Forcrand, H. Fukaya, A. Hasenfratz, S. Hashimoto, J. Kuti, M. Lüscher, A. Patella, F. Sannino, Y. Taniguchi, A. Tomiya and N. Yamada for useful discussions and comments. And we would like to thank A. Irie for making Fig. 10. We really appreciate T. Onogi and K. Higashijima for encouraging to release this paper.

Numerical simulation was carried out on NEC SX-8 and Hitachi SR16000 at YITP, Kyoto University, NEC SX-8R at RCNP, Osaka University, and Hitachi SR11000, SR16000 and IBM

System Blue Gene Solution at KEK under its Large-Scale Simulation Program (No. 09/10-22, 10-16, (T)11-12, 12-16 and 12/13-16), as well as on the GPU cluster at Osaka University and Taiwanese National Centre for High-performance Computing. We acknowledge Japan Lattice Data Grid for data transfer and storage. E.I. is supported in part by Strategic Programs for Innovative Research (SPIRE) Field 5. This work is supported in part by the Grant-in-Aid of the Ministry of Education (No. 22740173).

A. Raw data of TPL coupling constant

	$L/a = 6$		$L/a = 8$		$L/a = 10$	
β	g_{TPL}^2	# of Trj.	g_{TPL}^2	# of Trj.	g_{TPL}^2	# of Trj.
100.0	0.06304(31)	49500				
99.0			0.06369(27)	59500	0.06389(38)	39500
50.0	0.13229(49)	44000	0.13084(83)	49500	0.13349(93)	65500
20.0	0.3895(22)	72000	0.3910(31)	73000	0.3824(54)	49000
18.0	0.4512(34)	60000	0.4565(39)	83500	0.4513(60)	74000
16.0	0.5158(31)	108000	0.5282(53)	78500	0.5345(66)	88000
15.0	0.5739(44)	80000	0.5849(53)	100000	0.5863(68)	98500
14.0	0.6274(48)	90000	0.6492(66)	95500	0.6359(78)	120000
13.0	0.6944(59)	80000	0.7156(63)	106000	0.7357(93)	102500
12.0	0.7844(67)	90000	0.7930(75)	126500	0.8205(15)	80000
11.0	0.9154(93)	80000	0.9210(98)	126000	0.9939(19)	102500
10.0	1.050(14)	54000	1.071(18)	72000	1.129(25)	83500
9.5	1.120(13)	80000	1.161(15)	100000	1.172(23)	79600
9.0	1.225(15)	78000	1.279(15)	130500	1.352(29)	80000
8.5	1.303(15)	80000	1.380(18)	104400	1.433(28)	101000
8.0	1.530(19)	78000	1.570(35)	63500	1.612(40)	68000
7.5	1.603(19)	80000	1.710(27)	93600	1.770(33)	91000
7.0	1.812(23)	54000	1.924(22)	153000	1.987(31)	208000
6.7	1.893(23)	80000	2.079(30)	112000	2.078(39)	108200
6.5	1.968(32)	54000	2.109(30)	99000	2.226(43)	140000
6.3	2.108(29)	80000	2.235(27)	104000	2.336(45)	99400
6.0	2.206(25)	90000	2.383(42)	95000	2.476(40)	130000
5.7	2.339(29)	80000	2.503(34)	110000	2.589(51)	80000
5.5	2.436(31)	72000	2.660(50)	75000	2.804(56)	114800
5.3	2.546(29)	80000	2.765(39)	113000	2.908(57)	80000
5.0	2.716(37)	96000	2.917(61)	94000	3.147(69)	95000
4.7	2.790(39)	78000	3.101(52)	85000	3.380(72)	99200
4.5	2.810(35)	108000	3.219(55)	113000	3.599(76)	220400
4.3	2.942(34)	94000				
4.0	2.888(48)	69000				

Table A1 $L/a = 6, 8, \text{ and } 10.$ (Data set A)

	$L/a = 12$		$L/a = 16$		$L/a = 20$	
β	g_{TPL}^2	# of Trj.	g_{TPL}^2	# of Trj.	g_{TPL}^2	# of Trj.
99.0	0.06381(48)	36000	0.06331(72)	27900		
50.0	0.1316(11)	64800	0.1327(15)	60900	0.1336(13)	147100
20.0	0.3927(52)	86400	0.3956(62)	85800	0.4002(79)	123900
18.0	0.4463(61)	90000	0.469(14)	40000	0.4509(83)	148400
16.0	0.5463(97)	84600	0.5434(96)	116000	0.547(11)	155500
15.0	0.6110(12)	57200	0.601(12)	100600		
14.0	0.6478(13)	79200	0.641(12)	126000	0.637(13)	125900
13.0	0.7278(12)	99800	0.746(14)	101000		
12.0	0.8444(14)	102000	0.838(16)	118000	0.832(18)	258200
11.0	0.9601(19)	104000	0.956(23)	109800		
10.0	1.133(22)	159000	1.132(21)	186900	1.173(26)	263700
9.5	1.229(24)	128200	1.275(21)	227400		
9.0	1.315(24)	160500	1.376(33)	219100	1.427(33)	322400
8.5	1.479(27)	160600	1.523(27)	321000		
8.0	1.589(33)	104400	1.633(29)	379500	1.696(38)	295300
7.5	1.813(36)	169200	1.881(38)	279900		
7.0	2.058(40)	162400	2.112(45)	287700	2.077(45)	430700
6.7	2.168(35)	162600				
6.5	2.298(40)	212000	2.276(46)	466900	2.370(56)	301400
6.3	2.373(42)	181200				
6.0	2.498(46)	180000	2.662(57)	213600	2.625(67)	443700
5.7	2.678(46)	162800	2.860(57)	293400	2.901(60)	1892800
5.5	2.824(93)	64400	3.044(59)	387000	3.05(28)	262800
5.3	2.974(52)	191700	3.055(70)	457000		
5.0	3.235(64)	241800				
4.7	3.600(70)	262200				
4.5	3.57(12)	269500				

Table A2 $L/a = 12, 16,$ and 20 .(Data set A) (The data for $\beta = 5.5, L/a = 12$ becomes poor statistics since the bugged data was found after the simulations.)

B. Additional data set of TPL coupling constant for the local fit analysis

	$L/a = 6$		$L/a = 8$		$L/a = 10$	
β	g_{TPL}^2	# of Trj.	g_{TPL}^2	# of Trj.	g_{TPL}^2	# of Trj.
20.13	0.3892(17)	330200	0.3907(26)	188800	0.3975(42)	85500
17.55	0.4645(18)	353800	0.4658(31)	166700	0.4740(62)	88400
15.23	0.5647(29)	339500	0.5733(49)	170400	0.5671(86)	91600
13.85	0.6420(35)	352300	0.6522(55)	190000	0.6563(93)	83800
11.15	0.8818(55)	330100	0.8971(98)	164100	0.940(18)	112600
9.42	1.1443(60)	389300	1.191(10)	317200	1.237(14)	274700
8.45	1.3488(84)	289100	1.4204(70)	987600	1.444(14)	503900
7.82	1.5313(91)	383800	1.601(13)	344500	1.650(14)	454300
7.80					1.717(56)	45300
7.25					1.890(58)	54100
7.11			1.842(11)	720500	1.956(25)	256700
7.10			1.866(32)	78200		
6.85					2.068(60)	53900
6.80			1.984(34)	78000		
6.76	1.869(12)	306400	2.003(18)	356600	2.086(25)	305900
6.55			2.084(37)	78000		
6.47			2.1360(10)	1293000	2.220(25)	307200
6.45					2.380(69)	53700
6.25			2.313(47)	78100		
6.15					2.441(66)	47700
6.12	2.1429(95)	603000	2.307(18)	584700	2.434(35)	249700
5.95			2.317(64)	74800		
5.90					2.528(77)	47300
5.81	2.248(11)	530200	2.471(22)	415800	2.605(37)	216800
5.80			2.516(47)	78200		
5.53	2.408(11)	718600	2.676(29)	471800	2.784(46)	177000
5.36	2.489(10)	696700	2.698(66)	42900	2.820(65)	89400

Table B1 $L/a = 6, 8, \text{ and } 10.$ (Data set B)

	$L/a = 12$		$L/a = 16$	
β	g_{TPL}^2	# of Trj.	g_{TPL}^2	# of Trj.
20.13	0.3982(63)	83000	0.4138(75)	79800
17.55	0.4662(68)	85100	0.4780(92)	83600
15.23	0.588(12)	75200	0.566(14)	80700
13.85	0.674(14)	79100	0.699(19)	70800
11.15	0.914(13)	173700	0.962(30)	72500
9.42	1.263(19)	256200	1.228(29)	147600
8.45	1.470(18)	397200	1.520(25)	368200
7.82	1.670(26)	262300	1.695(52)	136300
7.11	1.966(30)	256800	1.996(40)	244700
6.76	2.095(34)	265700	2.163(65)	136400
6.47	2.278(29)	330900	2.391(50)	273100
6.12	2.562(36)	283200	2.489(62)	183700
5.81	2.723(45)	269100	2.729(79)	186000
5.53	2.950(56)	233600	2.953(83)	191200
5.36	3.030(50)	272600	3.06(10)	187200

Table B2 $L/a = 12$ and 16 . (Data set B)

C. Data set dependence, fit range dependence and the step scaling size dependence

We show the two kinds of result for the growth rate from the global fit analysis and local fit analysis in Sec. 7.1 and 7.2 respectively. They are consistent with each other within $1\text{-}\sigma$ although they have the difference data sets, the different fit range and fitting function each other. Here we would like to show the each systematic uncertainties.

The left top panel in Fig. C1 shows the data set dependence. The central analysis includes both Data sets in Appendix A and B, while the blue result is obtained by only Data sets in Appendix A, which is the same data sets with the global fit analysis. The results are consistent with each other within $1\text{-}\sigma$. The right top panel in the Fig. C1 shows the fit range dependence. The blue result is obtained by the data in the narrow β range; $\beta \leq 7.0$ for all lattice size. We can find the result is completely consistent with each other, and this local fit analysis is quite stable under the change of the fit range. Actually, we focus on the local β region where all data can be fitted by the linear or quadratic function in β . Such results can be expected when the data can be fitted well.

The bottom panel in Fig. C1 shows the result of $s = 2$ step scaling. Although the step scaling function depends on the step scaling parameter, the comparison for the position u^* must be independent of the step scaling parameter. We can find the position is consistent with that for $s = 1.5$, so that we can confidently conclude the existence of the fixed point and the interpolation works well in the $s = 1.5$ step scaling.

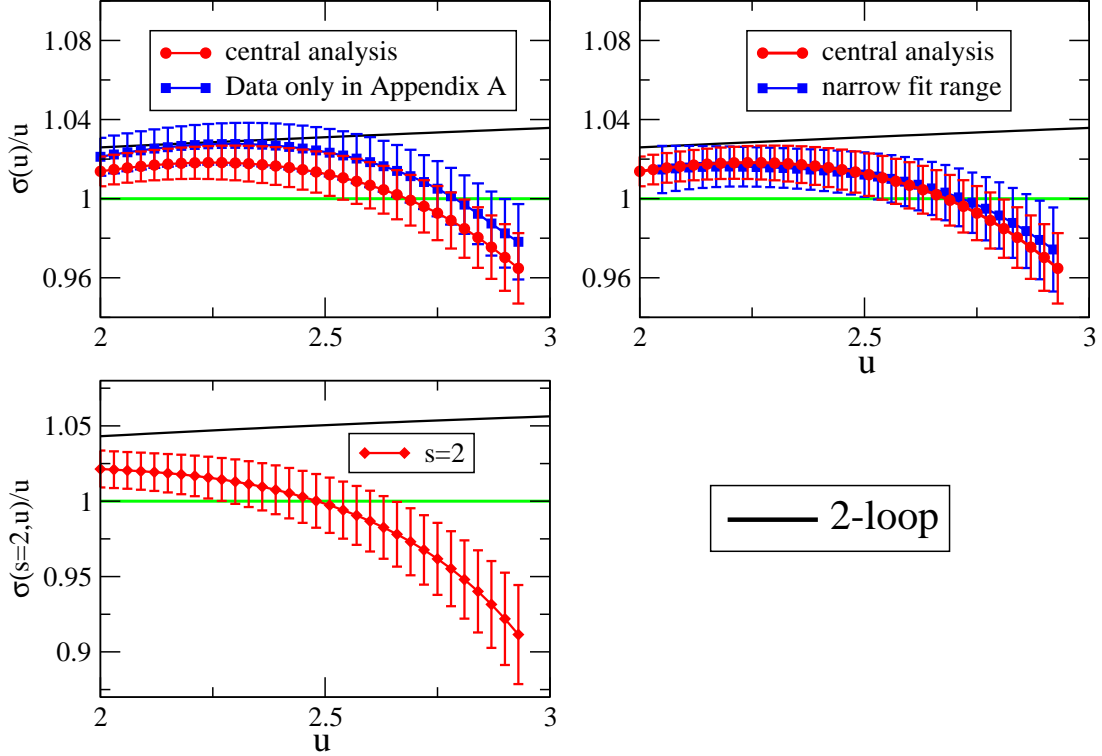


Fig. C1 The comparison for several local fit result. The top left panel shows the data set dependence. The top right panel shows the fit range dependence. The bottom panel shows the $s = 2$ step scaling, and then the comparison for the position of u^* shows the step scaling parameter dependence.

D. The effect of the nonuniform data on the global fit

The fixed point in this paper shows $u^* = 2.69$, however, the paper [59] shows $u^* \sim 2.0$. We consider that this difference comes from the mismatching the analysis method and the data sets quality in the paper [59]. In this appendix, we would like to consider the problem.

The data in the paper [59] are strongly concentrated around $\beta = 5.0$ and they are a part of Data set A and all data of set B. In the paper [59], the authors carried out the global fit analysis. As we mentioned in our guiding principle point 1, when we use the global fit in the broad β region by using a single fitting function, ideally the data do not favor a specific region. Our analysis for the global fit used only the data A in which each data has a similar accuracy and the interval of β is chosen to realize the almost constant growth rate of the renormalized coupling on the lattice. On the other hand, the data set B is strongly concentrated around $\beta = 5.0 - 6.0$ and a part of the data has quite high statistics in the high β region and for the small L/a . In this appendix, we would like to derive the global step scaling function by using the data in the both sets A and B and discuss the effect of the prejudiced data.

In Fig. D1, the results by using the data set A and the ones by using both A and B are shown in the top and bottom panels respectively. Each procedure of the step scaling is the same with the Sec. 7.1 and Sec. 7.2 for the global and local fit analysis respectively. Each red result in fig. D1 denotes the global fit analysis and the blue one denotes the local fit

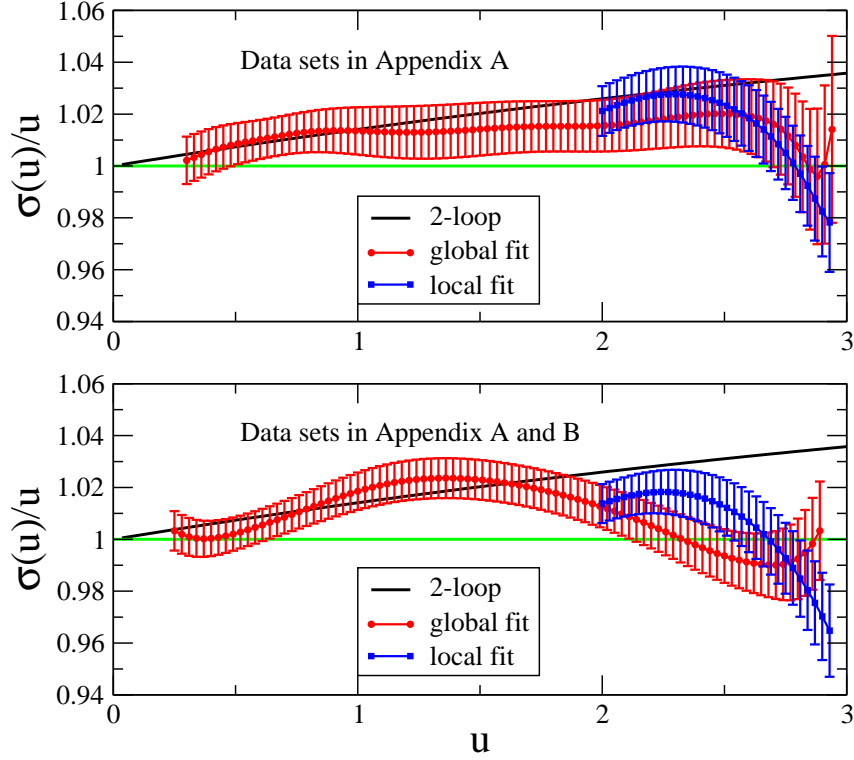


Fig. D1 The data set dependence and the fit range dependence. The top panel is obtained by only the data set A, and the bottom one is by the data sets A and B. Each red data denotes the global fit analysis and the blue one shows the local fit analysis. We can find the bottom panel shows the large fit range dependence.

analysis. The latter global fit result looks very similar with the result of the paper [59]. It shows the worse matching with the perturbative result, although still it is consistent with the perturbative prediction within the statistical error. The values u^* becomes smaller than the other ones with more than $2\text{-}\sigma$ discrepancy.

Now, we should consider which result is reliable. The global fit with the broad regime is always dangerous since the interpolated value includes non-vanishing contributions coming from the far region. To remove such effect we also carried out the local fit only with the focusing regime. The comparison the global fit result and the local fit result with both data A and B shows the larger fit range dependence rather than our central analysis in Fig. 17. The guiding principle point 1 must be important for such global fit analysis. That is the reason why we did not use the whole data of the data set B, when we would like to show the global behavior of the TPL running coupling constant.

E. Comments on the estimation method of the discretization effect

The discretization effect of the step scaling function $\Sigma(u, a/L; s)$ has two origins. The first one is a simple discretization effect of the renormalized coupling in the larger lattice size (sL/a). The second one comes from the tuned value of β to reproduce the input quantity u in the smaller lattice (L/a). When we take the continuum limit, we fixed the physical box size L and the lattice spacing a ($= \beta$), and then the leading term of the former ($O((a/sL)^2)$)

is smaller than the later one ($O((a/L)^2)$). So, it must be safe to avoid the interpolation of the small lattice sets if we consider the discretization effect seriously.

In our simulation, we have $L/a = 6, 8, 10, 12, 16$ and 20 . Then in the $s = 1.5$ step scaling we can take 4 data points to estimate the $O(a^2)$ effect with avoiding the small L/a interpolation, on the other hand $s = 2$ step scaling has only 3 data points. One of the advantages to use $s = 1.5$ step scaling is that there is the finest lattice data ($L/a = 12$). Furthermore the chi square fit with only one degree of freedom is strongly disturbed the statistical fluctuation, then we take the 4 points linear extrapolation as the central analysis in this paper.

In the paper [59], they carried out the interpolation for $L/a = 7$ by using $L/a = 6$ and 8 . However, the interpolation is dangerous since it is the coarsest two lattices interpolation. Actually, the raw data of the TPL (Figs. 13) shows the largest difference between $L/a = 6$ and 8 in the low β region and that must induce a large uncertainty of the interpolation. Furthermore, the estimation of the systematic uncertainty between 4 data points linear extrapolation for $L/a = 6, 7, 8, 10 \rightarrow 12, 14, 16, 20$ and 3 data points linear extrapolation for $L/a = 7, 8, 10 \rightarrow 14, 16, 20$ is nonsense, since the data of $L/a = 7$ is generated by $L/a = 6$ lattice data and thus the later extrapolation does not remove the effects of the coarsest lattice.

F. Eigenvalue of the Dirac operator

In this appendix, we report results for the measurement of the eigenvalue of the Dirac operator. We confirm two things from the quantity. At first, we show the global behavior of the eigenvalue. We find that the perturbative data is consistent with the tree level analysis in Sec. F.1. Furthermore, the β dependence of the data is smooth in the whole region and the data are inconsistent with zero even in the lowest β in our simulation parameter. These data also show that the theory is in the deconfinement and chiral symmetric phase. Secondly, we discuss the taste breaking in our simulation in Sec. F.2. In the case of the high β and the large lattice extent, the raw data of the low lying eigenvalues shows the degeneracy of the taste. In the strong coupling region, we take the continuum limit of the eigenvalue by using the TPL coupling constant as a reference of the same physics, and then we can show the effect of the taste breaking becomes mild in the continuum limit even in the strong coupling region.

This section is a preliminary report for the study on the eigenvalues of the Dirac operator. We will report the detailed studies in the independent paper in near future[69].

F.1. Perturbative analysis

Let us consider the massless staggered-Dirac operator $D(x, y)$,

$$D(x, y) = \sum_{\mu} \eta_{\mu}(x) \left[U_{\mu}(x) \delta_{x+\hat{\mu}, y} - U_{\mu}^{\dagger}(x - \hat{\mu}) \delta_{x-\hat{\mu}, y} \right], \quad (\text{F1})$$

where $\eta_{\mu}(x)$ is the staggered phase. This eigenvalues of D are pure imaginary since it is the anti-hermitian $D^{\dagger}(x, y) = -D(x, y)$:

$$D(x, y) \psi_{\lambda}^{(l)} = i \lambda^{(l)} \psi_{\lambda}^{(l)}, \quad (\text{F2})$$

where $\psi_{\lambda}^{(l)}$ denotes a Dirac fermion and (l) denotes the level of the eigenvalues. We define the lowest one as $l = 1$. The degree of freedom of one staggered-Dirac operator is 16, and

there are additional 3 color and 3 smell indices for our Dirac fermion (see: eq.(2.7)). The number of flavor ($N_f = 12$) is realized by (4 taste's) \times (3 smell's) degrees of freedom and there are 3 flavor (=smell) staggered Dirac fermions. The operator $D^\dagger D$ is hermitian and positive definite, and it can be decomposed to the operators on the even and odd sites. In this work, we measure the eigenvalues only positive and in the even-to-even sites, and then the degeneracy of one staggered-Dirac operator (4 taste's \times 4 spinor's) becomes half. The remain degrees of freedom (3 color's \times 3 smell's) can be counted as the unphysical twisted momenta in the twisted directions as explained in the Sec. 4.

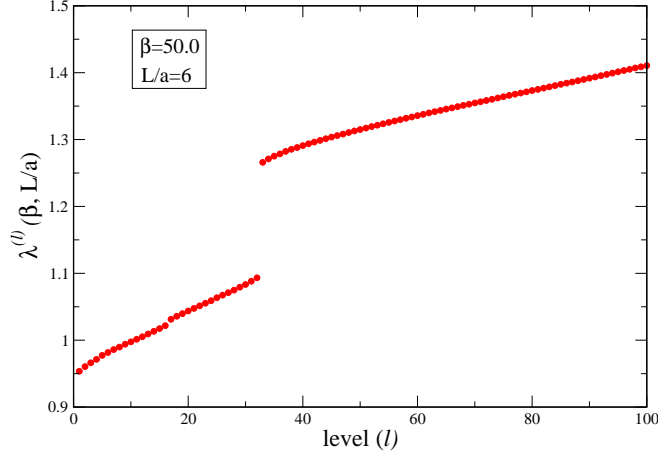


Fig. F1 The eigenvalues for $\beta = 50$, $L/a = 6$. The statistical error is the same size of the symbol.

At the tree level, we can calculate the eigenvalue of the Dirac operator on the lattice:

$$\lambda^2 = 4 \sum_{\mu} \sin^2 \frac{\hat{k}_{\mu}}{2}, \quad (\text{F3})$$

where \hat{k}_{μ} denotes the momentum of the fermion field for each direction. The leading order of $O(a)$ for low lying eigenvalues is proportional to the sum of \hat{k}_{μ} . In our simulation there is twisted boundary condition and the non-trivial vacuum phase, and then the momentum is given by the eq. (4.3) as \hat{k}_{μ}^{θ} . The lowest momentum is given in the following case of

$$\begin{aligned} (n_{\mu}^{ph}, n_{\mu}^{\perp}) &= (-1, 2) \text{ or } (0, 0) \text{ for both } \mu = x \text{ and } y, \\ n_{\mu}^{ph} &= 0 \text{ for both } \mu = z \text{ and } t. \end{aligned}$$

The degree of degeneracy for these momentum combinations is 4, and the sum of \hat{k}_{μ} is given by $\sqrt{10}\pi/\hat{L}$. The second lowest mode is given in the case of

$$\begin{aligned} (n_{\mu}^{ph}, n_{\mu}^{\perp}) &= (-1, 2) \text{ or } (0, 0) \text{ for } \mu = x \text{ or } y, \\ (n_{\mu}^{ph}, n_{\mu}^{\perp}) &= (-1, 1) \text{ or } (0, 1) \text{ for } \mu = y \text{ or } x \text{ (in same order),} \\ n_{\mu}^{ph} &= 0 \text{ for both } \mu = z \text{ and } t \end{aligned}$$

The degree of degeneracy of that is 8, and the sum of the momentum is $\sqrt{18}\pi/\hat{L}$. The third lowest mode is also counted, it is given by

$$\begin{aligned} (n_\mu^{ph}, n_\mu^\perp) &= (-1, 2) \text{ or } (0, 0) \text{ for both } \mu = x \text{ and } \mu = y, \\ n_\mu^{ph} &= 0 \text{ for } \mu = z \text{ or } t, \\ n_\mu^{ph} &= -1 \text{ for } \mu = t \text{ or } z \text{ (in same order)}. \end{aligned}$$

The number of degrees of degeneracy of that is 8, and the sum of the momentum is $\sqrt{22}\pi/\hat{L}$.

Let us compare the measured value of the simulation with this tree level analysis. The total degree of the degeneracy should be multiplied by 8, since we measure the eigenvalue of the staggered fermion on even-to-even site as we explained.

Figure F1 shows the first 100 eigenvalues in the $\beta = 50$, $L/a = 6$. There is a clear gap between $l = 32$ and $l = 33$ as we expected, although there is a large taste breaking since the lattice size is small. The ratio of the eigenvalue between first and 33rd levels is 1.328(2), and it is almost consistent with the tree level prediction $\sqrt{18/10}$. On the other hand, we cannot see the second gap, which we expect to lie between 96th and 97th levels. The numerical value of the ratio of them is 1.110(1), and the value is completely consistent with $\sqrt{22/18}$. Although the second gap is not clear, the eigenvalue reproduces the tree level prediction.

F.2. Global behavior of the eigenvalues and the taste breaking

We also measure the eigenvalue for all lattice parameters in the data sets in Appendix A. We show some examples in Fig. F2, in which the error is estimated by the bootstrap analysis. The eigenvalues of high β and the large lattice size show the 4-fold degeneracy, although there is large taste breaking in the small lattice size or low β region. The data at the lowest

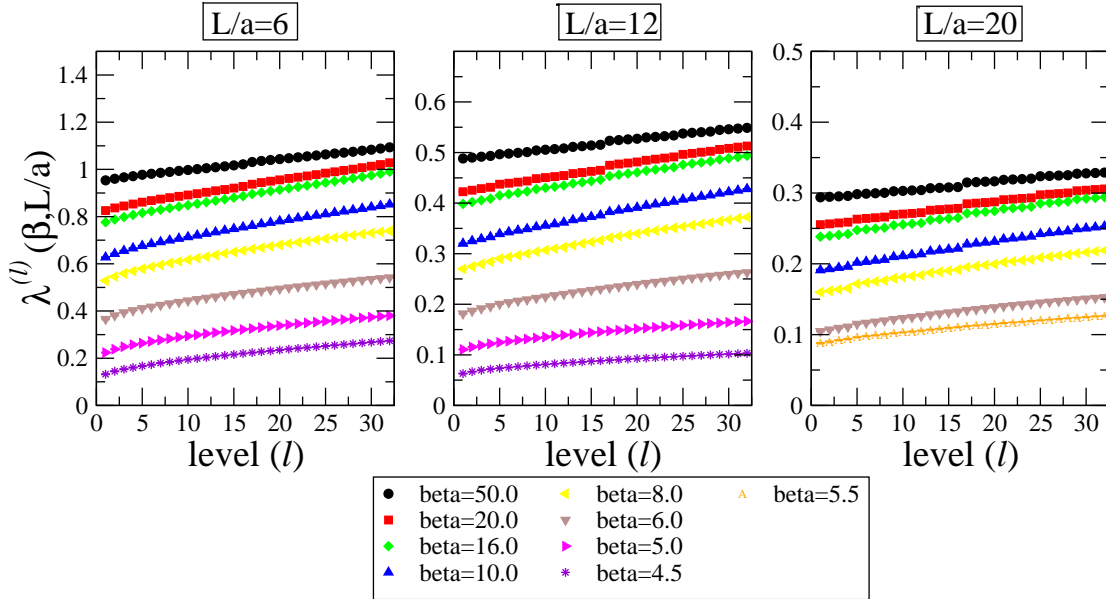


Fig. F2 The examples of the eigenvalues for several β and L/a . The statistical error is the same size of the symbol.

β , $\beta = 4.5$ for $L/a = 6, 12$ and $\beta = 5.5$ for $L/a = 20$, show the inconsistency with zero, and the β dependence of the data at fixed lattice extent is smooth in whole β region. If we assume that the Banks-Casher relation, and the chiral symmetry is also preserving even in the lowest β in our simulation parameter.

To see the taste breaking in our step scaling analysis in the strong coupling regime, we would like to show the eigenvalues in the continuum limit by taking the TPL renormalized coupling as a reference of the same physics:

$$L \cdot \lambda_{cont}^{(l)} \equiv \lim_{a \rightarrow 0} \hat{L} \cdot \lambda^{(l)}(\beta, L/a) \Big|_{g_{\text{TPL}}^2(L_0/L) = \text{const}}, \quad (\text{F4})$$

where the $(L \cdot \lambda_{cont})$ is dimensionless quantity and the scale L is defined by the value of the renormalized coupling constant. The figures F3 show the β dependence of the eigenvalues

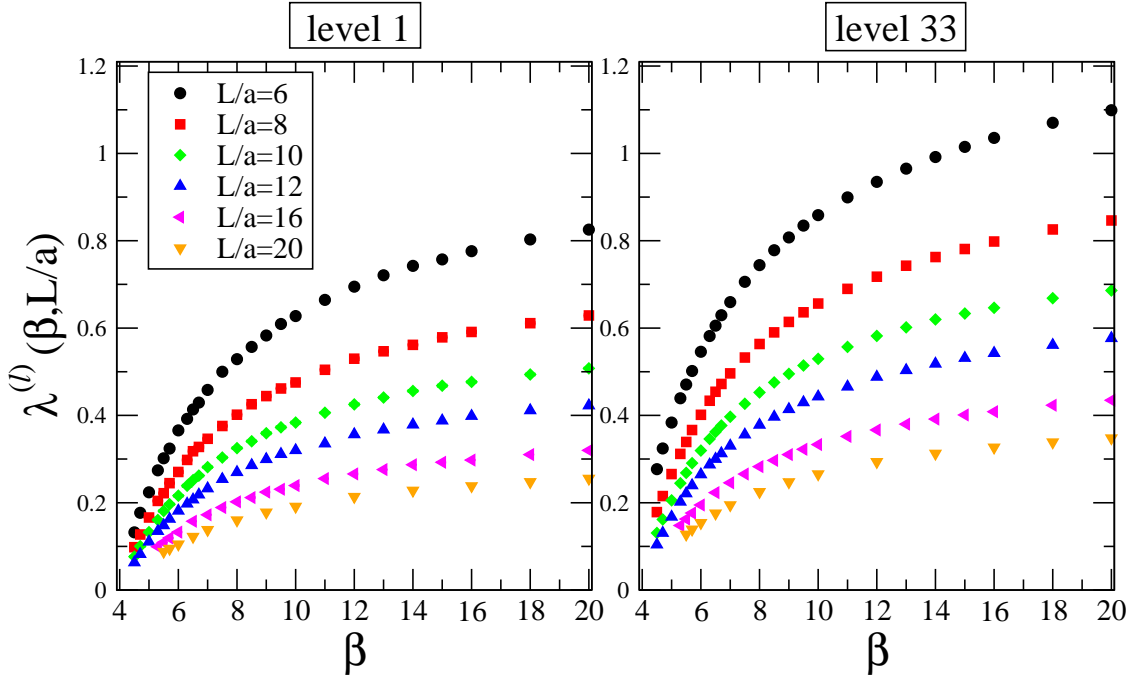


Fig. F3 The β dependence of the eigenvalues at the fixed L/a for the level 1 and 33. The statistical error is the same size of the symbol.

for the level 1 and level 33 for each lattice size. We fit the data at fixed level and lattice size in terms of β by the fitting function,

$$\hat{L} \cdot \lambda^{(l)}(\beta, L/a) = \sum_{i=0}^{N-1} c_i / \beta^i, \quad (\text{F5})$$

where N is the number of the fitting parameter, and in practical we choose the best fit value of N for each l and L/a . Typically, $N = 4 - 7$ are employed in this analysis.

In this analysis, the leading discretization error comes from the eigenvalue itself, which is proportional to $\hat{L} \cdot \lambda^{(l)} \propto \text{const.} + O(a^2)$ if the theory lives in the deconfinement phase. The other leading contribution $O(a^2)$ comes from the renormalized coupling, and the contribution comes via the tuned value of β . We take the continuum limit for 5 data points, $L/a =$

8, 10, 12, 16 and 20, and they can be fitted well by the linear function of $(a/L)^2$ in whole region. To estimate the systematic uncertainty of this continuum extrapolation we also show the quadratic extrapolation of $(a/L)^2$ for 6 data points included the coarsest lattice $L/a = 6$.

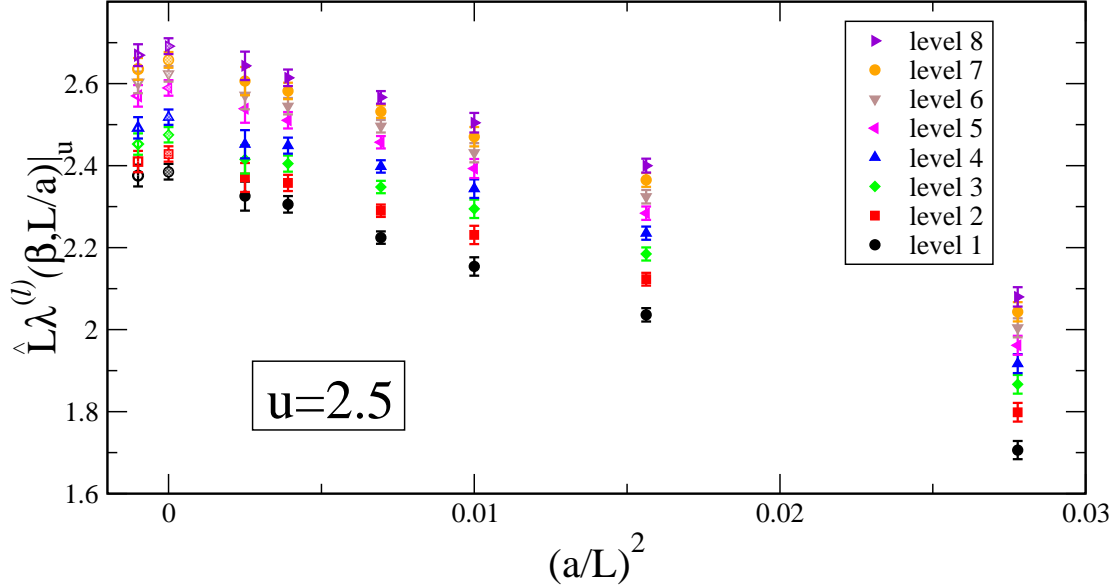


Fig. F4 The continuum extrapolation for the low lying eigenvalues for $u = 2.5$. Each full symbol denotes the eigenvalue at the interpolated β for each lattice size; $L/a = 6, 8, 10, 12, 16$ and 20 from the right to left. The shadow symbol at $(a/L)^2 = 0$ denotes the extrapolated value by the linear extrapolation function of $(a/L)^2$ for the finer 5 lattice data. The empty symbol at $(a/L)^2 = -0.001$ shows the extrapolated value for the quadratic function of $(a/L)^2$ by using all 6 data points.

As an example, we take $u = 2.5$, which corresponds to the region for $(\beta, L/a) = (5.4, 6) - (6.4, 20)$. The taste breaking of the raw data in these region is strong. The continuum extrapolation for $u = 2.5$ is shown in Fig. F4. In this plot, we show the eigenvalues at continuum limit for the low lying eigenvalues; level 1 – 8. The shadow symbol at $(a/L)^2 = 0$ denotes the extrapolated value for the linear extrapolation function of $(a/L)^2$ for the finer 5 lattice data. The empty symbol at $(a/L)^2 = -0.001$ shows the extrapolated value for the quadratic function of $(a/L)^2$ by using all 6 data points. The difference between these two kinds of the extrapolation can be identified as the systematic uncertainty. Including the systematic error, we find that the breaking of the level 1 – 4 becomes mild at the continuum limit even in the strong coupling regime.

References

- [1] E. Bilgici, A. Flachi, E. Itou, M. Kurachi, C. -J. D. Lin, H. Matsufuru, H. Ohki and T. Onogi *et al.*, PoS LAT **2009**, 063 (2009)
- [2] E. Itou, T. Aoyama, M. Kurachi, C. -J. D. Lin, H. Matsufuru, H. Ohki, T. Onogi and E. Shintani *et al.*, PoS LATTICE **2010**, 054 (2010)
- [3] T. Aoyama, H. Ikeda, E. Itou, M. Kurachi, C. -J. D. Lin, H. Matsufuru, K. Ogawa and H. Ohki *et al.*, arXiv:1109.5806 [hep-lat].
- [4] Y. Iwasaki, K. Kanaya, S. Kaya, S. Sakai and T. Yoshie, Phys. Rev. D **69**, 014507 (2004)

-
- [5] S. Catterall and F. Sannino, Phys. Rev. D **76**, 034504 (2007)
 - [6] S. Catterall, J. Giedt, F. Sannino and J. Schneible, JHEP **0811**, 009 (2008)
 - [7] S. Catterall, J. Giedt, F. Sannino and J. Schneible, arXiv:0910.4387 [hep-lat].
 - [8] T. Appelquist, G. T. Fleming and E. T. Neil, Phys. Rev. Lett. **100** (2008) 171607, [Erratum-ibid. **102** (2009) 149902], Phys. Rev. D **79** (2009) 076010
 - [9] T. Appelquist *et al.* [LSD Collaboration], Phys. Rev. Lett. **104**, 071601 (2010)
 - [10] T. Appelquist, G. T. Fleming, M. F. Lin, E. T. Neil and D. A. Schaich, Phys. Rev. D **84** (2011) 054501
 - [11] T. Appelquist, R. C. Brower, M. I. Buchoff, M. Cheng, S. D. Cohen, G. T. Fleming, J. Kiskis and M. Lin *et al.*, arXiv:1204.6000 [hep-ph].
 - [12] Z. Fodor, K. Holland, J. Kuti, D. Negradi and C. Schroeder, Phys. Lett. **B681**, 353-361 (2009).
 - [13] Z. Fodor, K. Holland, J. Kuti, D. Negradi and C. Schroeder, PoS LAT **2009**, 058 (2009)
 - [14] Z. Fodor, K. Holland, J. Kuti, D. Negradi and C. Schroeder, JHEP **0911**, 103 (2009)
 - [15] Z. Fodor *et al.*, Phys. Lett. B **703** (2011) 348
 - [16] A. Deuzeman, M. P. Lombardo and E. Pallante, Phys. Lett. B **670**, 41 (2008)
 - [17] A. Deuzeman, M. P. Lombardo and E. Pallante, Phys. Rev. D **82**, 074503 (2010)
 - [18] K. Miura, M. P. Lombardo and E. Pallante, Phys. Lett. B **710**, 676 (2012)
 - [19] A. Deuzeman, M. P. Lombardo, T. N. da Silva and E. Pallante, arXiv:1209.5720 [hep-lat].
 - [20] P. de Forcrand, S. Kim and W. Unger, arXiv:1208.2148 [hep-lat].
 - [21] X. -Y. Jin and R. D. Mawhinney, PoS LATTICE **2011**, 066 (2011)
 - [22] A. Hasenfratz, Phys. Rev. D **82**, 014506 (2010)
 - [23] A. Hasenfratz, arXiv:1106.5293 [hep-lat].
 - [24] A. Cheng, A. Hasenfratz and D. Schaich, Phys. Rev. D **85**, 094509 (2012)
 - [25] T. DeGrand and A. Hasenfratz, Phys. Rev. D **80**, 034506 (2009)
 - [42] T. DeGrand, Y. Shamir and B. Svetitsky, Phys. Rev. D **82**, 054503 (2010)
 - [27] T. DeGrand, Phys. Rev. D **84**, 116901 (2011)
 - [28] T. DeGrand, Y. Shamir and B. Svetitsky, Phys. Rev. D **85**, 074506 (2012)
 - [29] T. DeGrand, Y. Shamir and B. Svetitsky, arXiv:1201.0935 [hep-lat].
 - [30] Y. Aoki, T. Aoyama, M. Kurachi, T. Maskawa, K. -i. Nagai, H. Ohki, A. Shibata and K. Yamawaki *et al.*, Phys. Rev. D **86**, 054506 (2012)
 - [31] L. Del Debbio, A. Patella and C. Pica, Phys. Rev. D **81**, 094503 (2010)
 - [32] L. Del Debbio, B. Lucini, A. Patella, C. Pica and A. Rago, Phys. Rev. D **80**, 074507 (2009)
 - [33] L. Del Debbio, B. Lucini, A. Patella, C. Pica and A. Rago, Phys. Rev. D **82**, 014510 (2010)
 - [34] F. Bursa, L. Del Debbio, L. Keegan, C. Pica and T. Pickup, Phys. Rev. D **81**, 014505 (2010)
 - [35] L. Del Debbio and R. Zwicky, Phys. Rev. D **82**, 014502 (2010)
 - [36] F. Bursa, L. Del Debbio, L. Keegan, C. Pica and T. Pickup, Phys. Lett. B **696**, 374 (2011)
 - [37] L. Del Debbio and R. Zwicky, Phys. Lett. B **700**, 217 (2011)
 - [38] F. Bursa, L. Del Debbio, D. Henty, E. Kerrane, B. Lucini, A. Patella, C. Pica and T. Pickup *et al.*, Phys. Rev. D **84**, 034506 (2011)
 - [39] A. Patella, Phys. Rev. D **86**, 025006 (2012)
 - [40] M. I. Buchoff, Phys. Rev. D **85**, 074503 (2012)
 - [41] M. Hayakawa, K. I. Ishikawa, Y. Osaki, S. Takeda, S. Uno and N. Yamada, Phys. Rev. D **83** (2011) 074509
 - [42] T. DeGrand, Y. Shamir and B. Svetitsky, Phys. Rev. D **82**, 054503 (2010)
 - [43] J. Giedt and E. Weinberg, Phys. Rev. D **84**, 074501 (2011)
 - [44] J. Giedt and E. Weinberg, Phys. Rev. D **85**, 097503 (2012)
 - [45] A. J. Hietanen, J. Rantaharju, K. Rummukainen and K. Tuominen, JHEP **0905**, 025 (2009)
 - [46] A. J. Hietanen, K. Rummukainen and K. Tuominen, Phys. Rev. D **80**, 094504 (2009)
 - [47] T. Karavirta, A. Mykkanen, J. Rantaharju, K. Rummukainen and K. Tuominen, JHEP **1106**, 061 (2011)
 - [48] T. Karavirta, J. Rantaharju, K. Rummukainen and K. Tuominen, JHEP **1205**, 003 (2012)
 - [49] T. Karavirta, K. Tuominen and K. Rummukainen, Phys. Rev. D **85**, 054506 (2012)
 - [50] W. E. Caswell, Phys. Rev. Lett. **33**, 244 (1974).
 - [51] J. A. M. Vermaseren, S. A. Larin and T. van Ritbergen, Phys. Lett. B **405** (1997) 327
 - [52] T. Banks and A. Zaks, Nucl. Phys. B **196**, 189 (1982).
 - [53] M. Luscher, P. Weisz and U. Wolff, Nucl. Phys. B **359** (1991) 221.
 - [54] M. Luscher, R. Narayanan, P. Weisz and U. Wolff, Nucl. Phys. B **384** (1992) 168
 - [55] M. Luscher, R. Narayanan, R. Sommer, U. Wolff and P. Weisz, Nucl. Phys. Proc. Suppl. **30**, 139 (1993).
 - [56] G. M. de Divitiis, R. Frezzotti, M. Guagnelli and R. Petronzio, Nucl. Phys. B **422** (1994) 382
 - [57] G. 't Hooft, Nucl. Phys. B **153**, 141 (1979).
 - [58] M. Lüscher and P. Weisz, Nucl. Phys. B **266** (1986) 309
 - [59] C. -J. D. Lin, K. Ogawa, H. Ohki and E. Shintani, JHEP **1208**, 096 (2012)

-
- [60] G. M. de Divitiis, R. Frezzotti, M. Guagnelli and R. Petronzio, Nucl. Phys. B **433** (1995) 390 Nucl. Phys. B **437** (1995) 447
 - [61] G. Parisi, Published in Cargese Summer Inst. 1983:0531
 - [62] H. D. Trottier, N. H. Shakespeare, G. P. Lepage and P. B. Mackenzie, Phys. Rev. D **65** (2002) 094502
 - [63] G. de Divitiis *et al.* [Alpha Collaboration], Nucl. Phys. B **437**, 447 (1995)
 - [64] S. Capitani, M. Luscher, R. Sommer and H. Wittig [ALPHA Collaboration], Nucl. Phys. B **544** (1999) 669
 - [65] E. Bilgici, A. Flachi, E. Itou, M. Kurachi, C. -J D. Lin, H. Matsufuru, H. Ohki and T. Onogi *et al.*, Phys. Rev. D **80**, 034507 (2009)
 - [66] E. T. Tomboulis, arXiv:1211.4842 [hep-lat].
 - [67] T. A. Ryttov and R. Shrock, Phys. Rev. D **83** (2011) 056011
 - [68] M. Mojaza, C. Pica and F. Sannino, Phys. Rev. D **82**, 116009 (2010), C. Pica and F. Sannino, Phys. Rev. D **83**, 035013 (2011)
 - [69] E. Itou and A. Tomiya, in preparation